ACCEPTED MANUSCRIPT

Towards real-time 4D radiation dosimetry on an MRI-linac

Towards real-time 4D Radiation Dosimetry on an MRI-Linac

Y De Deene[1]§**, M Wheatley**[1]**, B Dong**[2]**, N Roberts**[2]**, U Jelen**[2]**,
D Waddington**[3]**, G Liney**[2]

5　[1] Department of Engineering, Faculty of Science, Macquarie University, Sydney,
Australia
[2] Ingham Institute, Liverpool, Australia
[3] ACRF Image X Institute, Faculty of Medicine and Health, The University of
Sydney, Sydney, Australia

10　E-mail: Yves.DeDeene@mq.edu.au

Abstract. 4D radiation dosimetry using a highly radiation-sensitive polymer gel dosimeter with real-time quantitative MRI readout is presented as a technique to acquire the accumulated radiation dose distribution during image guided radiotherapy (IGRT) on an MRI-Linac. Optimized T_2-weighted Turbo-Spin-Echo (TSE) scans are
15　converted into quantitative ΔR_2 maps and subsequently to radiation dose maps.

The concept of temporal uncertainty is introduced as a metric of effective temporal resolution. A mathematical framework is presented to optimize the echo time of the TSE sequence in terms of dose resolution, and the trade-off between temporal resolution and dose resolution is discussed. The current temporal uncertainty achieved with
20　the MAGAT gel dosimeter on a 1 T MRI-Linac is 3.8 seconds which is an order of magnitude better than what has been achieved until now.

The potential of real-time 4D radiation dosimetry in a theragnostic MRI-Linac is demonstrated for two scenarios: An irradiation with three coplanar beams on a head phantom and a dynamic arc treatment on a cylindrical gel phantom using a rotating
25　couch. The dose maps acquired on the MRI-Linac are compared with a treatment plan and with dose maps acquired on a clinical 3T MRI scanner. 3D gamma map evaluations for the different modalities are provided. While the presented method demonstrates the potential of gel dosimetry for tracking the dose delivery during radiotherapy in 4D, a shortcoming of the MAGAT gel dosimeter is a retarded dose response.
30　The effect of non-ideal RF pulses as a result of SAR limitations or B_1-field inhomogeneity on the TSE acquired ΔR_2 values is analysed experimentally and by use of computational modelling with a Bloch simulator.

§ Present address: School of Engineering, Faculty of Science, Macquarie University, Sydney, Australia

4D Radiation Dosimetry 2

1. Introduction

Image guided radiotherapy (IGRT) utilizes non-invasive imaging to increase the spatial precision and accuracy of radiotherapy. Recently, theragnostic MRI-Linac systems have been deployed that enable MRI imaging with high soft-tissue contrast before, during and after treatment without additional image coregistration. Ultimately, feedback of the recorded tumour motion with MRI to the linear accelerator (Linac) would enable synchronized delivery of radiation beams to the moving tumour volume.

The temporal nature of IGRT makes it difficult to assess the overall accuracy of the treatment. Indeed, a latency between the tumour motion and the moving treatment beam can cause more harm than a radiation delivery that does not accommodate for tumour motion. End-to-end 4D dose verification can play a crucial role in safeguarding IGRT delivered with an MRI-Linac.

Humanoid shaped polymer gel dosimeters have been applied successfully in end-to-end dosimetric validation of high-precision radiotherapy in three dimensions (De Deene *et al* 2000a, Vergote *et al* 2004, Baldock *et al* 2010). Polymer gel dosimeters consist of hydrogels in which acrylic monomers are dispersed. Upon exposure to ionizing radiation, a radiation-induced polymerization reaction occurs whereby the created polymer aggregates are fixated by the hydrogel matrix. We hereby present the first results of real-time MRI on a radiation-sensitive polymer gel dosimeter during radiation delivery on the Australian MRI-Linac.

To enable reliable, real-time 4D radiation dosimetry, the radiation dosimeter must meet different requirements:

(i) The dosimeter must have a high dose-MRI sensitivity so that a clinically realistic

4D Radiation Dosimetry   3

incremental dose is visible on a realistic time scale.

(ii) The dosimeter must exhibit a fast dose response and good stability.

(iii) The dosimeter should have a low dose rate dependence and energy dependence.

60 (iv) The dosimeter should be tissue equivalent.

(v) The dosimeter should preferably have an antropomorphic shape.

(vi) The dosimeter should preferably have a low temperature dependence.

In considering a gel dosimeter for real-time dosimetry, it is not sufficient that a
fast pulse sequence is used; A significant change in detected dose difference needs to be
65 visible between two successive image frames. Indeed, there is no point in obtaining scans
in sub-second time intervals if the incremental dose in a pixel that is read out between
these intervals can not be determined with sufficient dose precision. In other words,
spatial and temporal resolution need to be considered in relation to dose precision.

Previous studies also indicated the potential of gel dosimetry for real time 4D
70 dosimetry on an MRI-Linac. In one of these studies, a Fricke based gel dosimeter is
proposed (Lee et al, 2018). The Fricke gel dosimeter has a typical dose-R_1 sensitivity
of 0.039 s^{-1} Gy^{-1} . In another study, a vinylpyrrolidone based gel dosimeter (VIPET)
is used which has an R_2-dose sensitivity of 0.152 s^{-1}.Gy^{-1} (Pappas *et al* 2019). We
here demonstrate for the first time, that real-time dosimetry in an MRI-Linac is feasible
75 by use of a gel dosimeter consisting of Methacrylic Acid, Gelatin and the Anti-oxidant
Tetrakis(hydroxymethyl)phosphonium salt (MAGAT) which has a dose-R_2 sensitivity
of 4.5 s^{-1}.Gy^{-1}, 30 times more sensitive than the earlier suggested VIPET polymer gel
dosimeter and 115 times more sensitive than the Fricke based gel dosimeter.

In line with the concept of dose resolution, we introduce the concept of temporal

4D Radiation Dosimetry   4

80   uncertainty as a metric of the effective temporal resolution. The temporal uncertainty

enables a quantitative comparison between different methods. It will be shown that

in the study by Lee *et al* using the FOX gel dosimeter, the temporal uncertainty

is in the order of 106 seconds, in the study by Pappas *et al* using VIPET gel, the

temporal uncertainty is in the order of 27 seconds, while the temporal uncertainty with

85   the MAGAT gel dosimeter in this study is in the order of 3.8 seconds.

Dose dependent changes in spin-spin relaxation rate ΔR_2 are derived from the

signal intensities in Turbo-Spin-Echo (TSE) images before and during radiation. The

conversion of TSE signal intensities to ΔR_2 is performed on a pixel-by-pixel basis

resulting in ΔR_2 maps. The ΔR_2 maps are then converted to dynamic dose maps

90   by use of a ΔR_2-dose calibration plot. The standard deviation on the measured dose

values depends on the MRI pulse sequence that is used to extract the dose values.

The parameters in the pulse sequence can be optimized to achieve the highest dose

resolution for a particular gel dosimeter. Such an optimization equation has been

provided previously for a two-point spin-echo and a Multi-Spin Echo (MSE) sequence

95   (De Deene *et al* 1998, De Deene and Baldock 2002). A derivation of the optimization

equation for the new TSE based approach is presented in appendix A of this paper. The

dose resolution is used to calculate the temporal uncertainty.

A retarded dose response of the MAGAT gel dosimeter was found and its effect

on the acquired dose values during and after radiation has been described in appendix

100 B. A difference in R_2-dose-response acquired with the MSE method and TSE method

has been attributed to two mechanisms. The first mechanism is the effect of a dose

dependent longitudinal magnetization recovery and is scanner-independent. The second

mechanism is attributed to non-ideal excitation and refocussing pulses and is scanner-

4D Radiation Dosimetry 5

dependent. These mechanisms are discussed in detail and have been analysed using

105 numerical simulations based on the generalized Bloch-equations (appendix C).

The principle of 4D radiation dosimetry is illustrated by two different treatments in

two different phantoms: A three-beam radiation of an anthropomorphic head phantom

and a dynamic arc treatment on a cylindrical phantom. Because the Linac is static in

the current configuration of the Australian MRI-Linac, a rotating couch in which the

110 phantom is suspended has been constructed in-house to deliver the dynamic arc. R_2

maps post-treatment were also acquired on both the MRI-Linac and a clinical 3T MRI

scanner by use of an MSE sequence that are then converted to dose maps by use of

irradiated calibration samples. The recorded dose maps of the three-beam treatment

are compared with a calculated dose distribution extracted from the treatment plan

115 using a gamma analysis.

4D Radiation Dosimetry 6

2. Materials and Methods

Four different kinds of experiments were conducted on the MRI-Linac:

Experiment A. The dose-response on the MRI-Linac was illustrated by exposing calibration vials and a cylindrical gel phantom to a single radiation beam.

120 *Experiment B.* To validate the effect of phantom size on the dose-R_2 response, a vial filled with MAGAT gel was inserted in a spherical flask filled with MAGAT gel and was irradiated from the side.

Experiment C. To illustrate a clinical dose verification, two treatments were considered: A three-beam coplanar treatment on a head-shaped phantom, and a rotational 125 treatment whereby a beam was directed on a rotating cylindrical gel phantom.

Experiment D. Additional experiments were performed on test tubes filled with MAGAT gel to study the effect of the pulse sequence and imaging parameters on the dose-R_2 response.

Different gel batches were used and irradiation/scanning was conducted on different 130 days for each of these experiments.

2.1. Treatment Planning

The three-beam radiation treatment on the head phantom and arc treatment (experiment C) have been modelled in Pinnacle[3] V16.02 (Philips Healthcare, The Netherlands). A Solid Water® slab was in place when acquiring the commissioning 135 beam data and therefore is included in the model. By using the Solid Water® slab to remove the high electron contamination, the build-up region of the beam is also absorbed. This poses challenges to modelling, as the equations used in the planning

4D Radiation Dosimetry   7

system are intended for modelling this region. However at depths beyond 1 cm the

model agrees within 2% of the commissioning beam data (Jelen *et al* 2020). Synthetic

140 CT scans of the cylindrical phantom and anthropomorphic head phantom were generated

from an MRI scan by assigning CT numbers to theoretical values for air (-1000 HU),

glass (2200 HU) and MAGAT gel (40 HU) and the CT dicom was imported into the

treatment planning system.

In the case of the cylindrical phantom, a 2.6 cm × 2.6 cm square field was planned

145 with the beam isocentre off axis to the centre of rotation by 2.6 cm. The dose was

calculated for a single beam and it was then exported from the treatment planning

system and the accumulated dose from rotating the phantom every 9 degrees was

calculated in MATLAB®.

The head phantom was planned with 3 coplanar beams of size 2.6 cm × 2.6 cm

150 with 120 degree angular spacing. All dose calculations were performed with dose grid

resolution of 1 mm × 1 mm × 1 mm using the adaptive convolution algorithm.

2.2. Fabrication of MAGAT gel dosimeters

Polymer gel dosimeters (PGDs) based on 6%(wt) methacrylic acid and 8%(wt) gelatin,

referred to as MAGAT, were fabricated according to a recipe discussed elsewhere (De

155 Deene *et al* 2006a). The methacrylic acid solution and gelatin sol were mixed at

approximately 32 °C. The antioxidant Bis[tetrakis(hydroxymethyl)phosphonium] sulfate

(2 mM) was added when the solution was cooled down to approximately 30 °C. For

experiment A, a 1.4 litre cylindrical glass phantom (diameter 120 mm, height 120 mm)

was filled with MAGAT gel. For experiment B, a 300 ml spherical glass flask and a

160 long test tube with flat bottom (diameter 10 mm; length 200 mm) were filled with

4D Radiation Dosimetry   8

MAGAT gel. The test tube was then inserted in the spherical phantom (figure 8a).
For experiment C, a glass head phantom and a cylindrical flask were filled with 3.2
litres and 1.5 litres of MAGAT gel respectively. In addition to the large phantoms
used in experiments A-C, test tube vials were both filled with MAGAT gel of the same

165 batch which served as calibration samples. Only a set of calibration vials were used
in experiment D. Immediately after fabrication, all phantoms were stored in a closed
container at room temperature to avoid exposure to visible light.

2.3. Rotating Couch

Because the Australian MRI-Linac does not have a rotating gantry, the phantom

170 (experiment C) was rotated instead by use of an automated rotating head couch
which was constructed in-house. The rotating couch (figure 1) was constructed from
polycarbonate and was driven by a pneumatic stepper motor constructed from a nylon
and chopped carbon fibre 3D printed filament (Groenhuis and Stramigioli 2018). The
pneumatic motor does not contain any metal parts, making it perfectly MRI compatible.

175 The angular position is controlled by use of a microcontroller (Arduino Uno) that
controls 4 pneumatic valves which provide compressed air to each of the pistons of
the pneumatic stepper motor.

4D Radiation Dosimetry　　　9

(a)

(b)

(c)

(d)

(e)
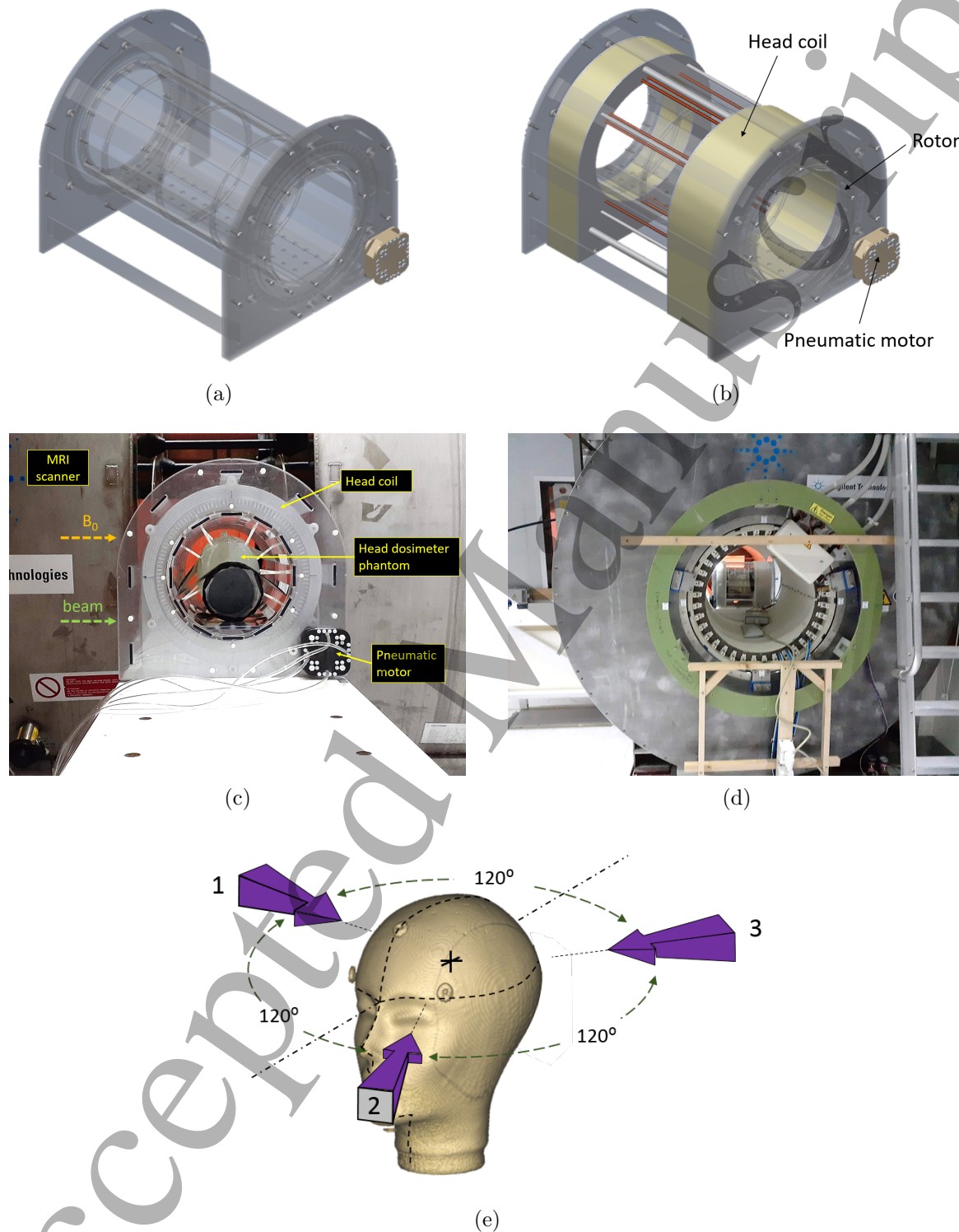
Figure 1: Rotating head couch for automated rotation of dosimeter phantoms inside the head coil. Schematic CAD drawings show the rotating head couch without (a) and with the head coil (b). The head dosimeter phantom is suspended inside the rotating couch using Nylon screws. The system is shown in two rotational positions, outside of the MRI (c) and inside the MRI scanner (d). The direction of the magnetic field and the radiation beam are also indicated (c). The beam directions with respect to the head phantom are indicated (e).

4D Radiation Dosimetry 10

2.4. Irradiation and MRI scanning

MRI scanning and radiation of the MAGAT PGDs was performed on the 1T Australian

180 MRI-Linac. The phantoms were also scanned between 6 hours and 26 hours post-radiation on a clinical 3T MRI (Siemens Verio). No active temperature compensation was applied during scanning or radiation.

2.4.1. Calibration Calibration vials were irradiated in a rectangular daily quality assurance (QA) water phantom at reference depth (10 cm) at a dose rate of 1 Gy/min

185 and a field size of 10 cm $\times$ 10 cm. In order to save beam time, two calibration samples were placed at any time inside the cylindrical cavity of the rectangular QA water phantom. After each radiation exposure, one of the samples was removed and replaced by a fresh sample and another incremental amount of radiation was delivered. This procedure was repeated until all calibration samples received incremental amounts

190 of radiation dose in steps of 0.5 Gy. The fact that a smooth calibration plot (with correlation coefficient ≤ 0.9995) was obtained, indicates no significant dependence of the dose-R_2 response with this fractionation scheme. This may seem in contrast with a previous study that found a dependence of the dose-R_2 response on fractionation in MAGAT PGDs (Karlsson *et al* 2007). However, it needs to be noted that the

195 dose delivered to every calibration vial was obtained in mostly two and at most three fractions and that the dose in each fraction was not equal which is different from many equal fractions. It is also important to note that in the study of Karlsson *et al* , a different dose rate per fraction (5.1 Gy/min) and different photon energy (18 MV) was applied. An alternative way to obtain a calibration plot is by irradiating a phantom

200 with a square radiation beam of which the dose distribution has been well-characterized

4D Radiation Dosimetry								11

(Oldham 1998). The advantage of this method is that it is fast as only a single beam

is given. The disadvantage is that it relies strongly on the prior characterization of the

dose distribution of the beam in contrast to the 'test tube'-approach where calibration

vials are irradiated under reference conditions as calibration vials can be placed in the

205 rectangular QA water phantom at the same location as the ionization chamber. It is

a misconception that the square beam approach would be more precise (De Deene and

Baldock 2002).

The R_2 values of the calibration samples are acquired by use of a 32-echo MSE

sequence with an echo time spacing between 10 ms and 20 ms (De Deene and Baldock

210 2002). R_2 maps were reconstructed from the 32 spin echo images using in house

developed Matlab® software code and using a non-linear least-square fit (De Deene

et al 1998). In the fit, only signal values that exceed 3 times the noise level were

considered in the fit, to avoid any bias in estimated R_2 values as a result of Rician

distributed noise at low signal levels (De Deene and Baldock 2002).

215 *2.4.2. Dynamic dosimetry* Dynamic scans of the dosimeter phantom were then

acquired on the MRI-Linac using a TSE sequence during radiation delivery (figure 2c).

After radiation delivery, additional R_2 maps were acquired with an MSE sequence on

both the MRI-Linac and the 3T MRI scanner. The dynamic TSE scans were converted

to R_2 difference maps that display the change in R_2 since the start of the radiation

220 treatment (figure 2c). Assuming that the effect of T_1 relaxation on the signal intensity

is negligible, the signal intensity in each voxel of the TSE scans can be described by a

simple exponential decay function.

$$S = S_0 e^{-R_2 \cdot TE} \tag{1}$$

4D Radiation Dosimetry   12

where S_0 is the signal intensity for the echo time TE approaching zero. The dose related

225 change in R_2 in a voxel receiving a dose D can then be easily derived from the signal

intensities before and after radiation as:

$$\Delta R_2 = \frac{1}{TE} ln \left(\frac{S(0\ Gy)}{S(D)} \right) \tag{2}$$

where $S(D)$ is the signal intensity in the same voxel after absorbing an amount of

radiation dose D and $S(0\ Gy)$ is the signal intensity in a voxel before radiation.

230 The dose D can then be easily derived by use of a calibration plot between ΔR_2 and

D which was obtained from the calibration samples (figure 2b). The assumption that

the T_1 effect can be ignored is only satisfied for sufficiently long repetition times that

allow full recovery of the longitudinal magnetization ($TR > 3T_1$) or in the case that T_1 is

not altered as a result of the radiation-induced polymerization. The effect of radiation-

235 induced changes in T_1 for realistically short repetition times on the signal intensity is

shown in section 3.2 and discussed in section 4.3. A correction factor accounting for

both the T_1 effect and sequence related discrepancies (see section 3.2) between MSE-

and TSE-derived R_2 values is applied (figure 2d) in the conversion of ΔR_2 maps to dose

maps (2e).

240 The Signal-to-Noise Ratio (SNR) in images was determined by using a region-of-

interest (ROI) in a homogeneous region of the image. Determination of the SNR in the

base images (T_2 weighted images) was performed in unexposed images where the signal

intensity was above 5 times the noise level, to avoid any bias as a result of a deviation

from the Gaussian distribution (De Deene 2004).
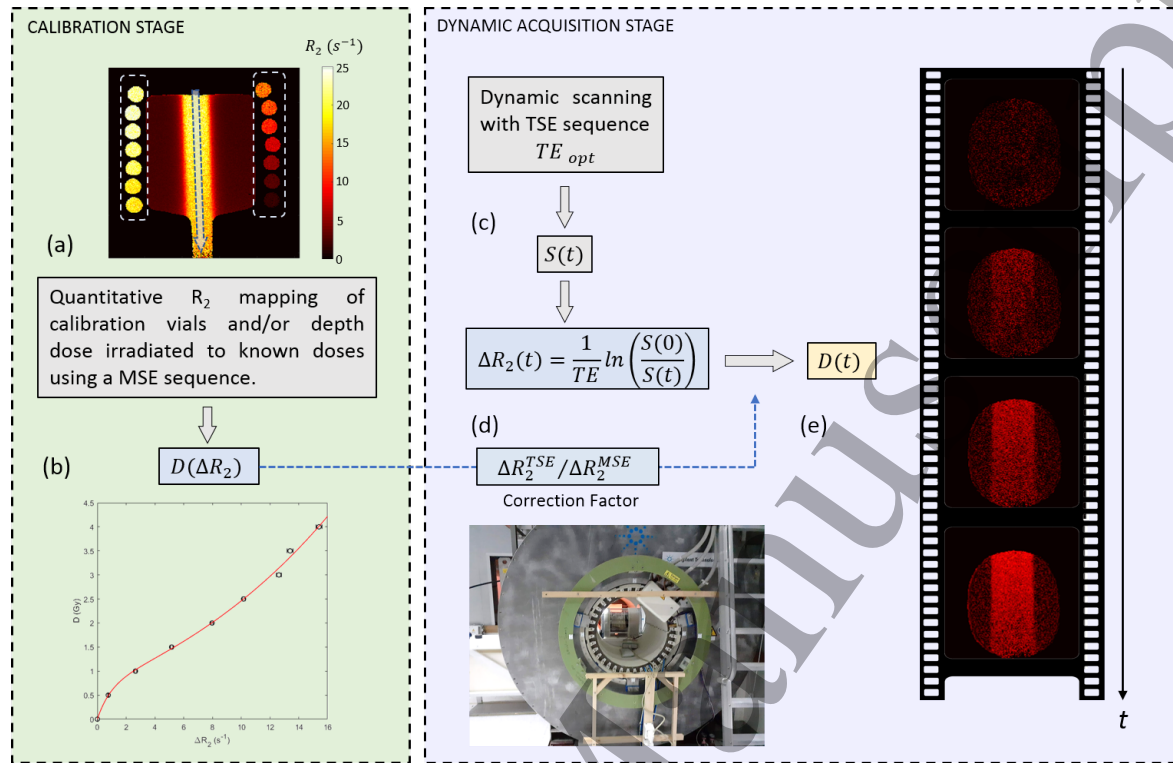
Figure 2: Outline of the procedure for converting a set of dynamically recorded T_2-weighted TSE MRI scans to dose maps. After exposing a set of calibration vials to preset dose values, an R_2 map is recorded using a multi-spin echo (MSE) sequence (a). A ΔR_2-dose calibration plot is then extracted from the average R_2 values within ROIs drawn in the calibration vials. Alternatively, a flask of gel can be irradiated with a square field of which the depth-dose profile is recorded with an ionization chamber or diamond detector (a). In the latter case, the ΔR_2-dose relation is extracted by use of a correlation scatter plot between the measured R_2-depth profile and the known dose profile (b). ΔR_2 is calculated from the ratio of the T_2-weighted TSE MRI scans before radiation and the T_2-weighted TSE MRI scans during radiation (c). The ΔR_2-dose relation is corrected for the difference between ΔR_2 acquired with a TSE sequence and ΔR_2 acquired with the MSE sequence (d). Dose maps are obtained for each of the T_2-weighted TSE MRI scans (e) by use of the corrected calibration plot (b).

4D Radiation Dosimetry 14

245 *2.4.3. Experiment A* In this initial experiment, a 1.4 L cylindrical gel phantom (diameter 12 cm) was irradiated with a 2 cm × 2 cm square 6 MV photon beam at a dose rate of 100 cGy/min. The high surface dose, which has been previously observed on the Australian MRI-Linac (Roberts *et al* 2019 and Jelen *et al* 2020), was mitigated by including a 2 cm slab of Solid Water® 5 cm upstream from the phantom.

250 The phantom was scanned dynamically using a Turbo-Spin-Echo (TSE) sequence for a total time span of 15 minutes. During this time span, the radiation beam was on for 4 minutes. TSE images were recorded with a square field-of-view (FOV) of 171 cm, a matrix size (MS) of 256 × 256 pixels, a slice thickness (Sl.Th) of 5 mm. The turbo factor (TF) was 22 and the effective echo time (TE) 272 ms. The receive bandwidth per 255 pixel (BW_{pix}) was 275 Hz. The repetition time (TR) was 2 seconds and two averages were taken per image to improve the SNR, resulting in a total measurement per scan of 48 seconds. Between each scan there was an additional time delay of 2 seconds, resulting in a scan frame rate of 50 s. The phantom was also scanned with an MSE sequence on the MRI-Linac and on the 3T MRI Linac with sequence parameters as listed in table 1).

260 *2.4.4. Experiment B* The spherical phantom with tube insert was irradiated with a 4 cm × 4 cm square 6 MV photon beam directed perpendicular to the longitudinal direction of the test tube at a dose rate of 100 cGy/min. The phantom was scanned dynamically with the TSE sequence at 15 second intervals for a total time span of 15 minutes. During scanning, the beam was switched on for 3 minutes. The phantom was 265 scanned with a MSE sequence on both the MRI Linac and the 3T MRI scanner. All scanning parameters are listed in table 1.

4D Radiation Dosimetry   15

2.4.5. Experiment C   A head-shaped dosimeter phantom was irradiated with 3 coplanar

beams at similar fluence rates (figure 1). Also, a 2 cm slab of Solid Water® was placed

between the beam and the phantom.   The angular separation between each of the

270 coplanar beams was 120° which was obtained by use of the automated rotating couch.

Prior to the dosimetry experiment, the rotating couch system was tested on the head

phantom on which fiducial markers were taped and the rotational accuracy was found

to be ±3 degrees. During the delivery of each beam, the head phantom was scanned

at 5 slice locations separated by 10 mm, using a TSE pulse sequence with imaging

275 parameters as listed in table 1. The time between two consecutive scans was 11 seconds

with 10 seconds effective scanning and 1 second delay time.

Another 1.5 L cylindrical gel phantom (diameter 11 cm) was inserted in the rotating

couch and irradiated with a lateral 2.6 cm × 2.6 cm beam that was placed 2.6 cm off

axis with respect to the cylindrical phantom. The 2 cm slab of Solid Water® was

280 placed between the beam and the phantom. The phantom was rotated by the automated

rotating couch over 360 degrees in incremental steps of 9 degrees every 18 seconds, while

the beam was kept on during the entire treatment. The time to rotate the phantom

over 9 degrees was 1.5 seconds. TSE scans were taken at every angular incremental

step with imaging parameters as listed in table 1 resulting in a total imaging time per

285 frame of 10 seconds. The time between two consecutive scans at different angles was

18 seconds. Additional MSE scans were recorded on both the MRI-Linac and 3T MRI

scanner with the sequence parameters specified in table 1.

For the three-beam experiment on the head phantom, a volumetric gamma-analysis

was conducted between the final TSE derived dose maps, the MSE derived dose maps on

290 the MRI Linac and the treatment plan. The gamma-analysis was developed in house in

4D Radiation Dosimetry 16

Matlab®. For the arc treatment on the cylindrical gel phantom, polar dose maps were reconstructed and radial and angular dose profiles were compared to TPS calculated dose profiles.

2.4.6. *Experiment D* To investigate the relation between the TSE acquired dose and the MSE required dose, a set of calibration vials were irradiated to doses between 0 and 5 Gy in steps of 0.5 Gy. The phantoms were scanned with both the TSE sequence and the MSE sequence on both the MRI-Linac and the 3T MRI scanner (Table 1). In addition, R_1 $(1/T_1)$ of the samples was determined by use of a spin echo sequence with TE = 20 ms and different repetition times (TR = 652 ms, 1000 ms, 1500 ms and 5000 ms). To determine the R_1 value, the signal versus TR is fitted against the signal equation:

$$S = S_0(1 - Ce^{-R_1 \cdot TR}) \tag{3}$$

where S_0 is the signal corresponding with the net magnetization and C accounts for imperfect refocussing pulses.

4D Radiation Dosimetry 17

Table 1: MRI scanning parameters for the different experiments. For all experiments, 5 slices were recorded for each scan. 'TE' refers to the effective echo time in the case of a TSE sequence and to the echo time spacing in the case of an MSE sequence. The Echo Train Length (ETL) refers to the turbo factor in the case of a TSE sequence and the number of T_2-weighted scans in the case of an MSE sequence. The acronyms 'MRL' and '3TMRI' correspond with 'MRI Linac' and '3T MRI Verio' respectively. T_{scan} is the total scan time.

Scanner Type	Exp.	Seq.	FOV (mm)	MS	Sl.Th. (mm)	TR (ms)	TE (ms)	ETL	BW_{pix} (Hz)	T_{scan}
MRL	A	TSE	171×171	256×256	5	2000	272	22	275	48 s
MRL	A	MSE	171×171	256×256	5	2000	15	32	130	8 min 32 s
MRL	B	TSE	200×200	192×192	5	1000	124	13	260	15 s
MRL	B	MSE	171×171	256×256	5	2000	15	32	130	8 min 32 s
MRL	C-Head	TSE	220×200	128×128	10	1000	160	13	130	11 s
MRL	C-Head	MSE	200×200	192×192	10	3620	20	32	130	11 min 35 s
MRL	C-Arc	TSE	150×150	128×128	10	1000	171	13	130	15 s
MRL	C-Arc	MSE	192×192	192×192	10	3500	16	32	130	11 min 12 s
MRL	D	TSE	180×180	128×128	10	1000	variable	variable	130	2 min 8 s
MRL	D	MSE	150×150	192×192	10	3620	20	32	130	11 min 35 s
3TMRI	A	MSE	171×171	256×256	5	3000	14	32	130	12 min 48 s
3TMRI	B	MSE	121×150	208×256	5	3000	10	32	271	10 min 24 s
3TMRI	C-Head	MSE	200×200	192×192	10	3620	20	32	130	11 min 35 s
3TMRI	C-Arc	MSE	180×180	256×256	5	10000	15	32	130	42 min 40 s
3TMRI	D	MSE	66×99	128×192	10	3000	15	32	151	6 min 24 s

3. Results

3.1. Radiation response of the polymer gel dosimeter

The dose-R_2 response curves for four different batches of MAGAT gel are shown in figure 3. The four dose-R_2 response curves correspond with the batches used in the four different experiments (A-D). The dose-R_2 response satisfies a bi-exponential relation. To convert the measured R_2 values to dose, an inverse relation needs to be derived. The inverse of a bi-exponential function is not trivial. Here, either a numerical inversion can be applied. Alternatively, a heuristic fit can be applied. It was found that a bi-exponential function provides an adequate fit for the R_2-dose relation (equation 4).

$$D = a + b \cdot e^{c \cdot R_2} - d \cdot e^{-e \cdot R_2} \tag{4}$$

where the fit coefficients a, b, c, d and e are all real positive. The R_2-dose calibration

4D Radiation Dosimetry   18

plots for the different experiments on the MRI-Linac and the 3T MRI scanner are shown

in figure 3b and d respectively.
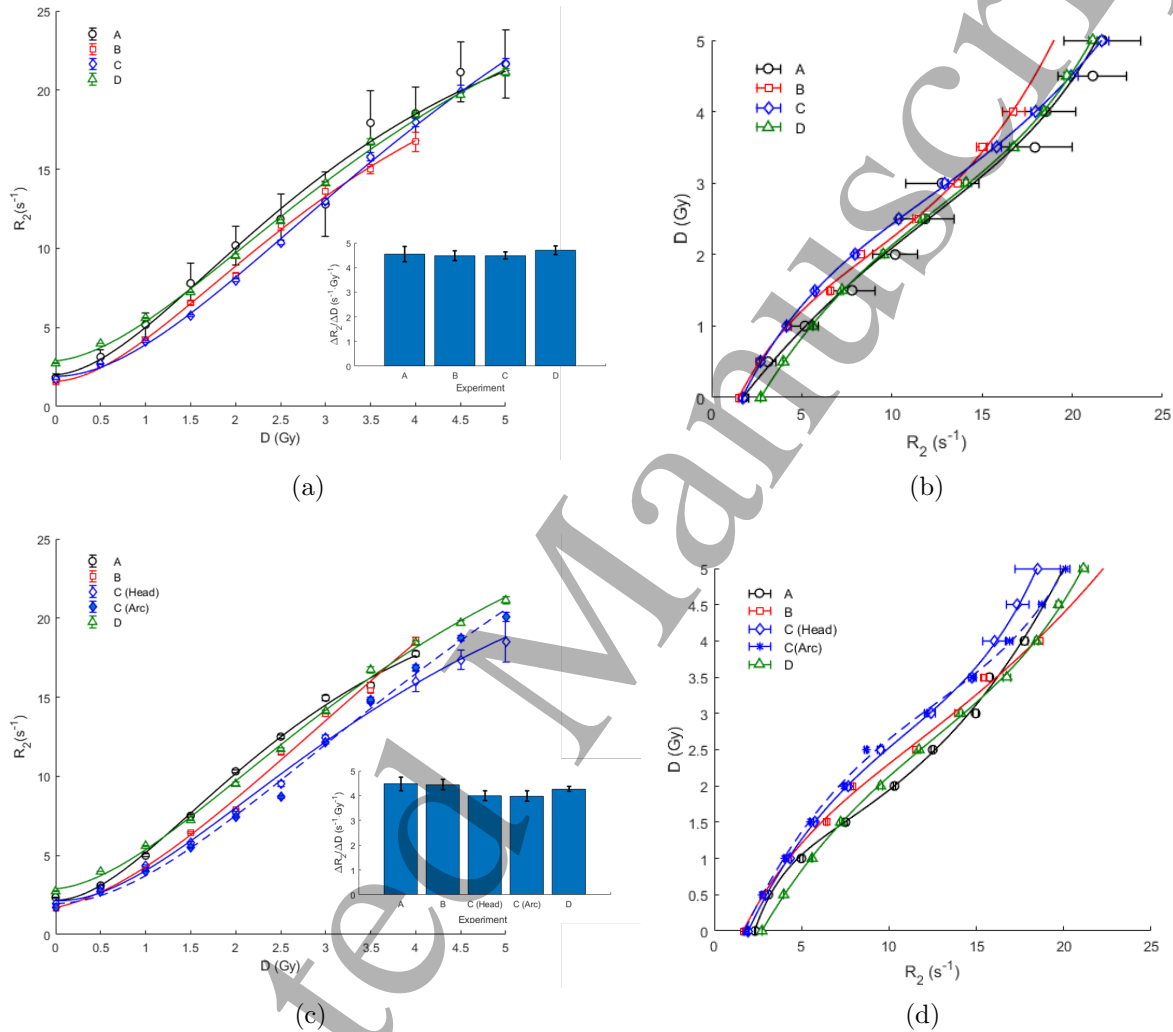
Figure 3: Dose-R_2 response plots (a,c) and corresponding R_2-dose calibration plots (b,d) for the different experiments on the MRI-Linac (a,b) and on the 3T MRI scanner (c,d). The inset figures show the dose sensitivity extracted in the linear region of the dose-R_2 curve [1 Gy, 3.5 Gy]. The error bars in the inset figure correspond with an uncertainty on the fit of one standard deviation. A: Single beam experiment; B: Phantom size experiment; C: Treatment experiment; D: MSE versus TSE experiment. On the 3T MRI scanner, calibration vials were scanned twice for experiment C (same batch): once together with the head phantom and another time with the cylindrical phantom. The latter measurement is indicated as filled diamond symbols with corresponding fit as a dashed line.

A measure of the dose-R_2 sensitivity can be obtained by considering the slope in a

4D Radiation Dosimetry   19

linear region of the response curves ([1 Gy, 3.5 Gy]) and is found to be 4.55 $s^{-1}.Gy^{-1}$

320   on the MRI Linac and 4.23 $s^{-1}.Gy^{-1}$ on the 3T MRI scanner (inset figure 3a and c).

Some increase in R_2 after switching off the radiation beam was observed. Figure 4

shows the corresponding change in registered dose as a function of time in a region of

interest in the phantom from experiment B. Similar temporal changes were found in

the other experiments. It can be seen that the retarded response not only results in an

325   increase after radiation but also in a smaller rate of dose registration in the first seconds

when the radiation beam is switched on.
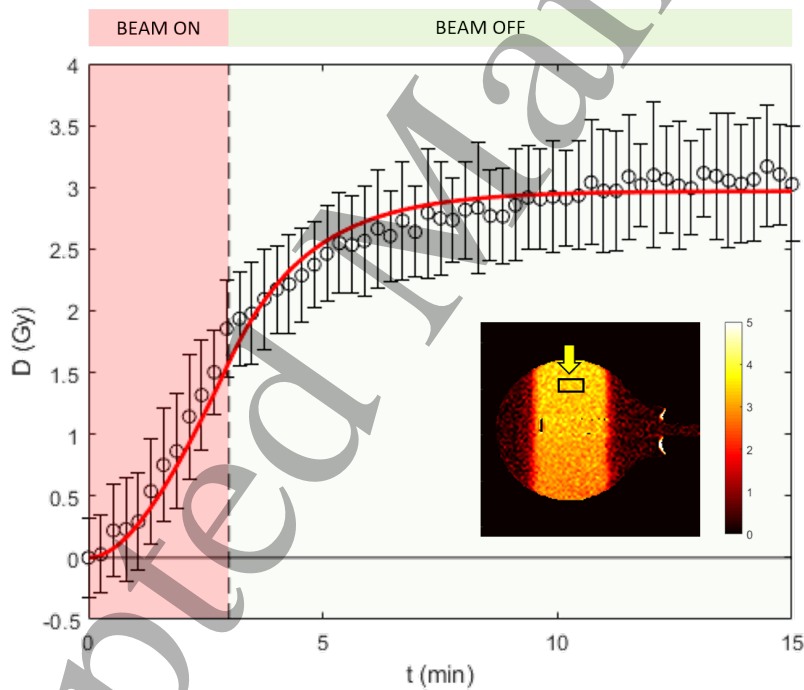
Figure 4: Temporal change in registered dose during and after radiation. The time constant fitted on the retarded response function was found to be $\tau = 83s$. The inset picture shows a dynamic recorded dose map frame of a spherical phantom indicating the ROI where the dose response was extracted. Error bars correspond to standard deviations inside the ROI.

To model the retarded response, a first order kinetic response is considered

4D Radiation Dosimetry　　　　　　　　　　　　　　　　　　　　　　　　20

(appendix B). During radiation the registered dose D_r is given by

$$D_r(t) = \dot{D}t + \dot{D}\tau_r(e^{-t/\tau_r} - 1) \tag{5}$$

330　while after radiation, the registered dose is described by

$$D_r(t) = D - \dot{D}\tau_r e^{-t/\tau_r}(e^{t_{rad}/\tau_r} - 1) \tag{6}$$

where $\dot{D}$ is the dose rate, τ_r is the characteristic time constant for the retarded response, D is the total absorbed dose and t_{rad} is the duration of the radiation. For a derivation of equations 5 and 6, the reader is referred to appendix B. By fitting the registered dose

335　to equations 5 and 6, the characteristic time for the retarded response τ_r was found to be 83 s.

3.2. Effect of sequence parameters on the dose calculation

In applying equation 1, it is assumed that the repetition time TR is very large with respect to TE. However, in order to acquire images with relatively short measurement

340　times, TR is shortened below full longitudinal magnetization recovery. The equation for signal intensity is then given by

$$S = S_0 e^{-R_2 \cdot TE}\left(1 - 2e^{-R_1\left(TR - \frac{TE}{2}\right)} + e^{-R_1 \cdot TE}\right) \tag{7}$$

Note that if the relaxation rate R_1 would be independent of dose, equation 2 would still be valid as the factor between brackets cancels out in both the numerator and

345　denominator of equation 2. However, as can be seen from figure 5d, the spin-lattice relaxation rate R_1 is dose dependent. A significant difference between R_1 measured on the 1T MR-Linac and R_1 measured on the 3T MRI scanner is also clearly visible (figure 5d). If the repetition time is decreased or the echo time is increased, the T_1 effect in the factor between brackets of equation 7 increases.

4D Radiation Dosimetry   21

350   MSE and TSE measured ΔR_2-dose response curves are shown in figures 5a and

b for the 3T MRI scanner and the MRI-Linac respectively. A discrepancy of 15% is

found between ΔR_2 measured with the MSE sequence and ΔR_2 measured with the

TSE sequence on the 3T MRI scanner (figure 5a), while a discrepancy of 40% is found

on the MRI-Linac (figure 5b). To investigate if the discrepancy is caused by ignoring

355   the aforementioned T_1 effect, the signal intensity was calculated using equation 7 for

the same echo time ($TE = 170\ ms$) and repetition time ($TR = 1\ s$) applied in the dose

experiments. The corresponding theoretical ΔR_2, affected by incomplete longitudinal

magnetization recovery, were derived by applying equation 2. These theoretical ΔR_2

values (affected by the T_1 effect) are shown as blue dashed curves in figures 5a and 5b.

360   It can be seen that the discrepancy in ΔR_2 measured with the MSE sequence and TSE

sequence on the 3T MRI scanner is close to the expected ΔR_2 values when the T_1 effect

is taken into account (figure 5a). At higher dose values (D > 3.5 Gy), the TSE measured

ΔR_2 deviates from the predicted ΔR_2 on the 3T MRI scanner. This may be explained

by another effect which is related to the low signal intensity in the TSE images at high

365   dose levels. If the signal in the TSE image after radiation $S(D)$, drops below 5 times

the noise level ($S(D) \leq 5\sigma_S$), the non-Gaussian characteristic of the noise starts to play

a role which will result in a further underestimation of ΔR_2, hence of the registered

dose. If the signal in the TSE image is lower than 5 times the noise level, the noise

follows a Rician distribution and the signal intensity is overestimated. Consequently,

370   the calculated change in R_2 will be underestimated.

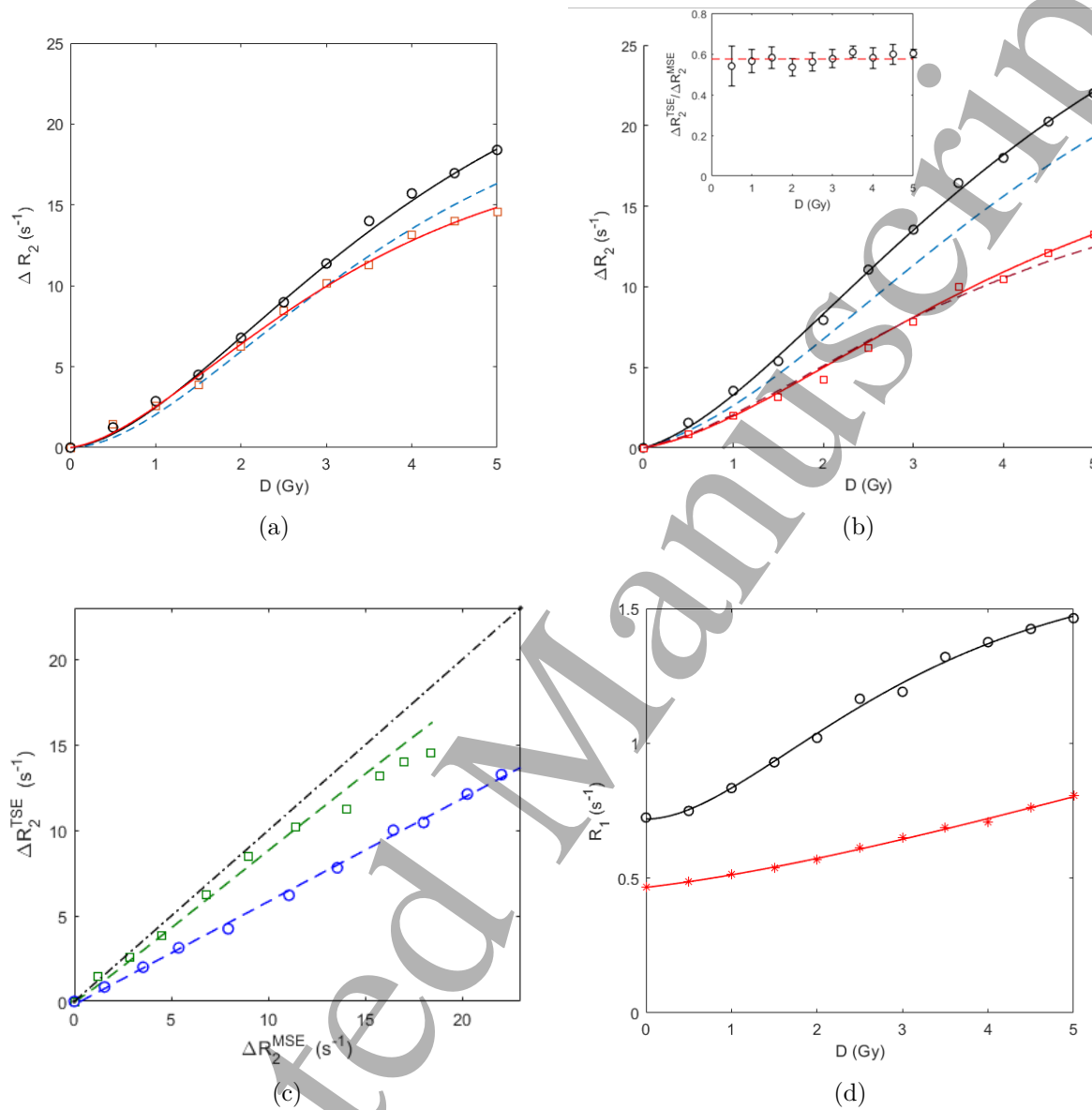*4D Radiation Dosimetry*

22

(a)

(b)

(c)

(d)

Figure 5: ΔR_2 versus dose plot obtained with a MSE sequence (black circular symbols) and using the TSE sequence (square red symbols) on the 3T MRI scanner (a) and the MRI-Linac (b) revealing a larger discrepancy between the TSE measured ΔR_2 and MSE measured ΔR_2 on the MRI-Linac. The dashed blue line corresponds with the MSE derived ΔR_2 values but taking incomplete longitudinal relaxation into account and the red dashed line corresponds with the Bloch simulated response curve with non-ideal transmit voltages. The red and black solid line in (a) and (b) are bi-exponential fits to the measured TSE and MSE measured ΔR_2 values respectively.The inset figure in b shows the ratio of TSE and MSE derived ΔR_2 values. A correlation plot of ΔR_2 measured with MSE and TSE on the MRI-Linac (blue circular symbols) and on the 3T MRI scanner (green square symbols) is shown in c. Identity correlation is shown as a dot-dashed black line. Longitudinal relaxation R_1 as a function of dose measured on the 1 T MRI-Linac (black circular symbols) and on the 3 T MRI scanner (red stars) (d).

4D Radiation Dosimetry   23

However, the larger discrepancy of 40% between MSE and TSE measured R_2 values

on the MRI-Linac can not be explained by the T_1 effect or the noise contribution alone.

It was found that the ratio between ΔR_2 measured with the TSE sequence and ΔR_2

measured with the MSE sequence is independent of the relaxation rate (inset figure in

375 5b). As TSE measured ΔR_2 correlates with the MSE measured ΔR_2 by a scaling factor

of 0.575, a correction factor of 1.74 ($= 1/0.575$) can be applied on the TSE measured

dose distributions. A more comprehensive MRI study revealed that imperfect excitation

and refocusing pulses on the MRI-Linac are the cause of the discrepancy in TSE and

MSE measured ΔR_2 values (see appendix C).

380 The influence of the turbo factor in the TSE sequence was also investigated

experimentally on the 3T MRI scanner. It was found that the turbo factor (TF) did

not have any significant effect on the acquired R_2-dose response when varied from 13 to

30 (figure 6).

(a)   (b)
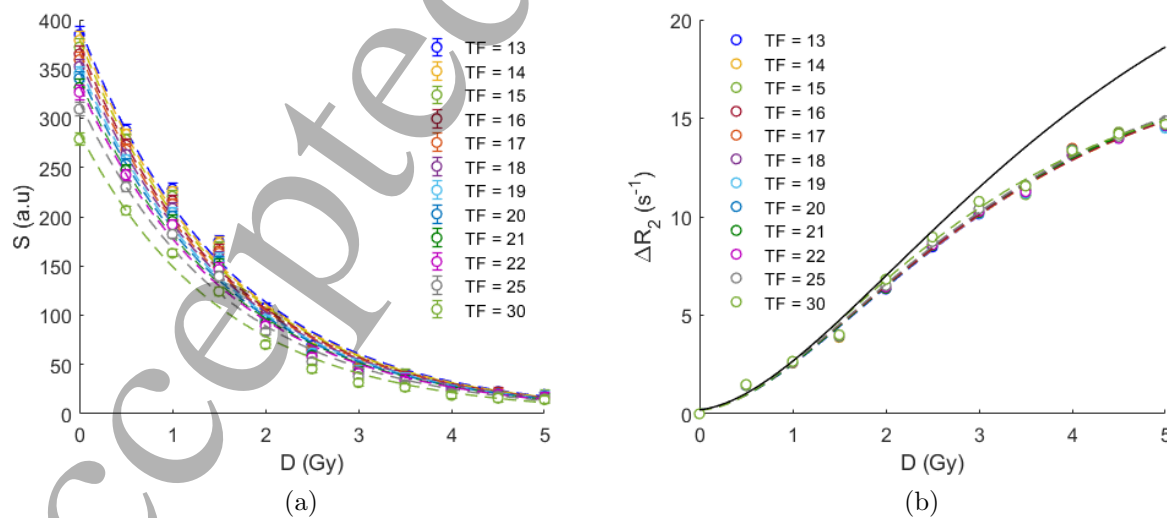
Figure 6: The effect of the turbo factor (TF) on the acquired ΔR_2 in the TSE sequence. While an increase in turbo factor results in a change in signal intensity (a), no significant change in ΔR_2 (b) is seen. The black solid line in (b) displays ΔR_2 acquired with the MSE sequence.

4D Radiation Dosimetry 24

3.3. Single beam experiment (experiment A)

385 A time series of measured dose maps of a single radiation beam demonstrate a rapid response during radiation and a smaller increase after radiation (figure 7). Depth-dose profiles and lateral dose profiles at 5 cm depth are extracted from the dose maps in figure 7a and are shown in figure 7b and c respectively. The depth-dose profiles are extracted by averaging dose values in the lateral direction (along x) over a width of 390 1 cm and lateral profiles are extracted by averaging dose values in the longitudinal direction of the beam (along z) over a 2 cm region. TPS derived depth-dose profiles are shown as solid lines in figure 7b. While the manifestation of absorbed dose can be appreciated from the recorded dose maps, it is clear from the dose profiles in figure 7b, that the noise in the dose maps is relatively high with the noise increasing as the dose 395 increases. The signal-to-noise ratio (SNR) in an unexposed raw TSE image was found to be 9.15 resulting in a relatively poor dose resolution in the dose maps. Comparing the expected TPS calculated depth-dose profiles with the gel measured depth-dose profiles, it can be seen that the recorded dose is lagging behind the delivered dose in agreement with the observations of retardation in section 3.1. The lateral profiles are fit against 400 the function:

$$D(x) = D_0 \frac{\sinh(\zeta a)}{\cosh(\zeta a) + \cosh(\zeta x)} \tag{8}$$

where ζ is a parameter related to the penumbra width and a is half the width of the beam.

A video of the acquired dose formation of an irradiation of calibration vials and of 405 the single radiation beam during and after radiation can be found in the supplementary material ($\rightarrow$ MOVIE 1, MOVIE 2).

4D Radiation Dosimetry 25

(a)

(b)

(c)
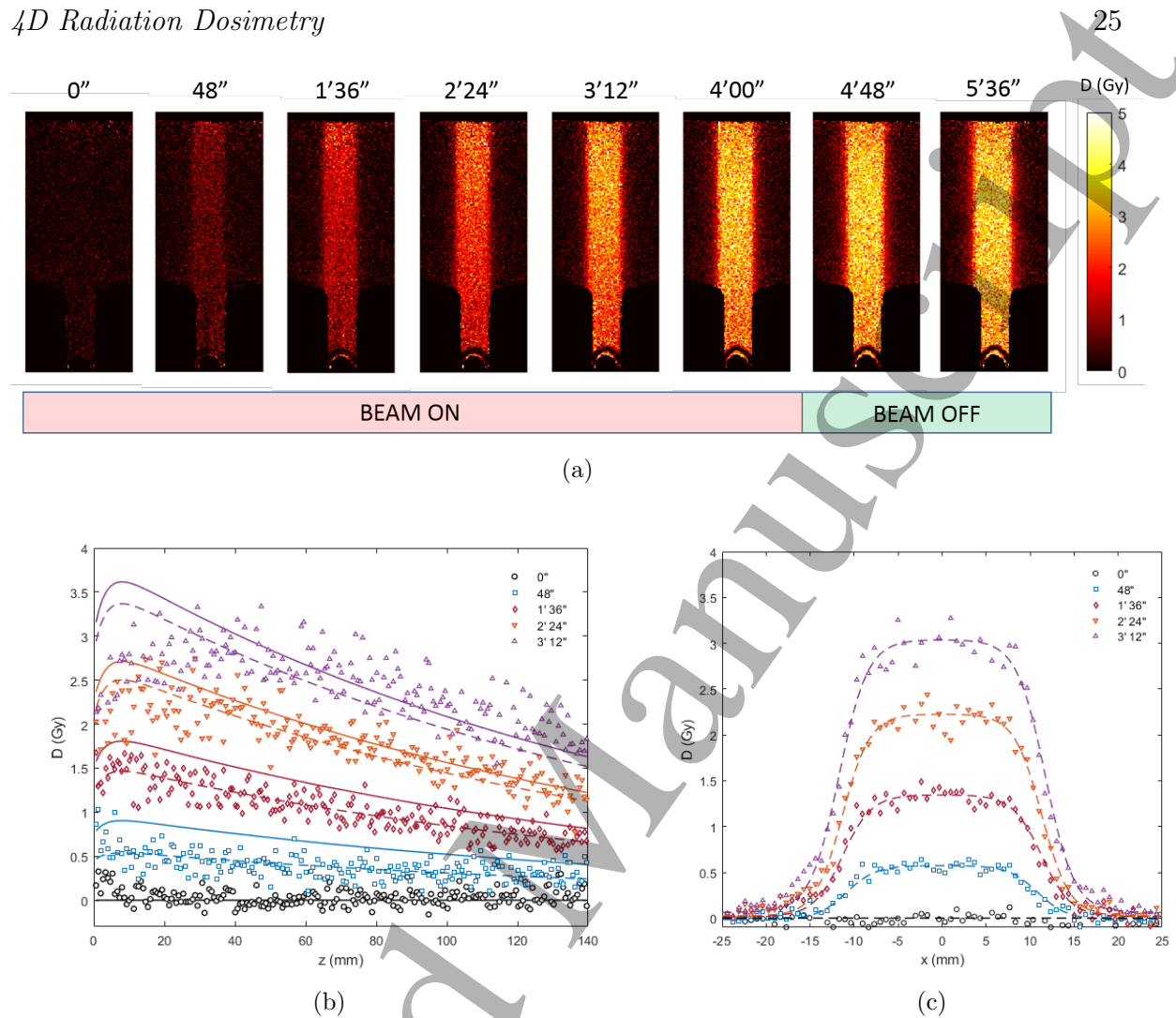
Figure 7: Dose maps recorded dynamically during radiation delivery of a single 2 cm × 2 cm beam (a) and corresponding depth-dose profiles (b) and lateral profiles at 5 cm depth (c). Solid lines indicate expected dose profiles without retardation and dashed lines correspond with scaled theoretical dose profiles.

3.4. Phantom size experiment (experiment B)

No significant change is observed between the dose registered outside and inside the test tube on the MRI-Linac during radiation or after radiation (figure 8b-d). A video of the acquired dose formation during and after radiation can be found in the supplementary material (→ MOVIE 3).

High resolution R_2 maps acquired with the MSE sequence on the 3T MRI scanner 18 hours post-radiation show a 15% increase in registered dose along the entire beam

4D Radiation Dosimetry   26

but no significant difference in registered dose between the inner region of the test tube

415 and the outside of the test tube (figure 8e). However, a 13% overestimation of the dose

within 1 mm of the glass wall can be observed.
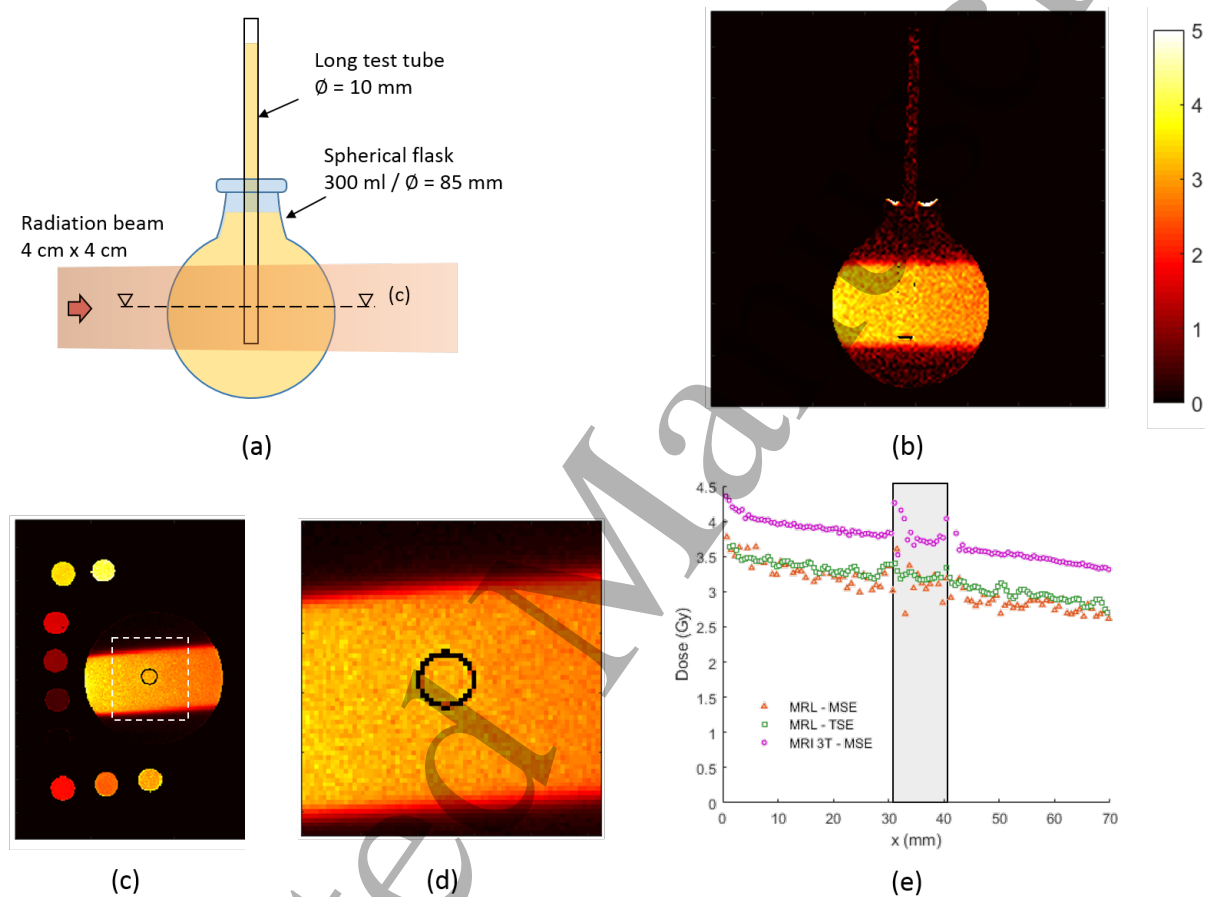
Figure 8: Dose maps of a spherical gel flask with inserted test tube. Drawing of the radiation set-up (a). Average of the last 16 dose frames of the dynamic TSE scans (coronal slice) (b) and dose map acquired with the MSE sequence on the MRI-Linac (c). Calibration tubes surrounding the spherical flask are also visible. A zoomed area around the inserted test tube shows that the dose in the test tube is not affected (d). Depth-dose profiles obtained with the three different methods (e): Multi-Spin-Echo sequence on the MRI-Linac (MRL - MSE); Turbo-Spin-Echo sequence on the MRI-Linac averaged over the 16 last dose frames (MRL - TSE); Multi-Spin-Echo sequence on the 3T MRI scanner (3T MRI - MSE).

4D Radiation Dosimetry   27

3.5. 3D dose experiment: Head phantom (experiment C)

Dose maps acquired at different time intervals during radiation are shown in figure 9.
The signal-to-noise ratio (SNR) in an unexposed TSE image was found to be 24.
420 Between different beams, R_2 maps were also acquired with the MSE sequence (not
shown). A movie of the dose formation during treatment delivery in the five slices can
be found in the supplementary material ($\rightarrow$ MOVIE 4: The five slices correspond to the
dose maps acquired at 10 mm separation and arranged from left to right in the cranial
to caudal direction. The middle (third) slice is acquired at the isocentre).
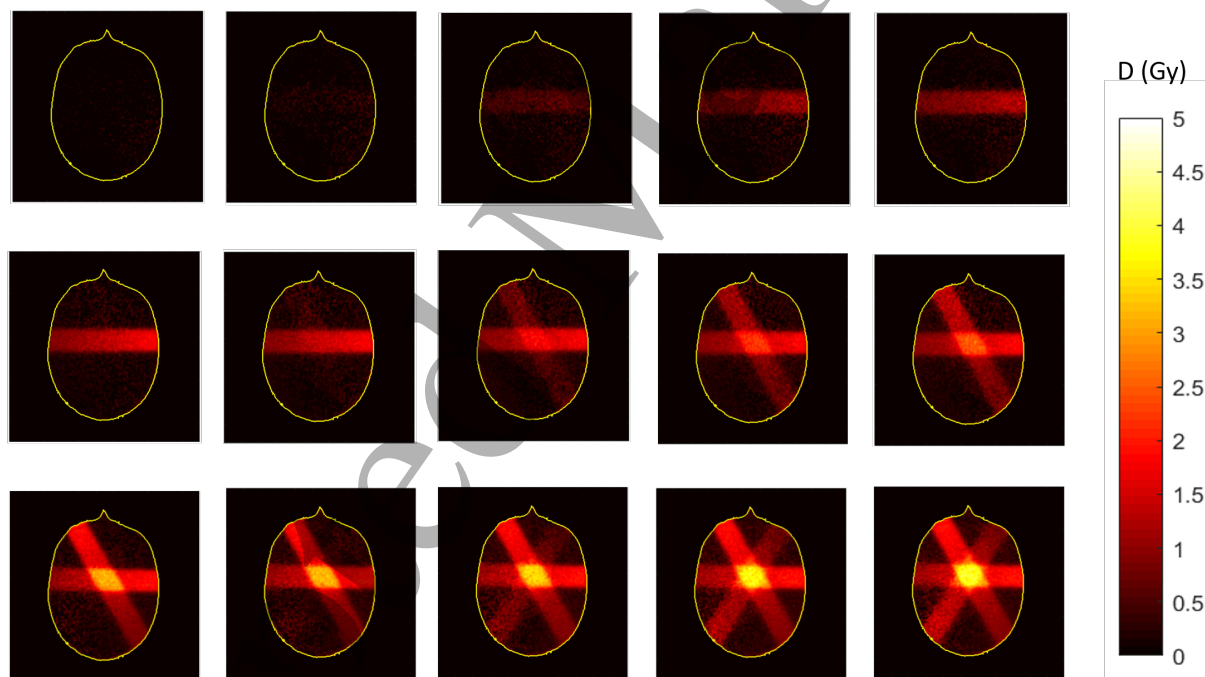
Figure 9: Dose maps of the central slice recorded dynamically on the MRI-Linac during
radiation delivery of three 2.6 cm x 2.6 cm beams on a head phantom. The FOV of the
dose maps is 220 mm × 220 mm. The time between two adjacent images in a row is 44
seconds (every 4th recorded frame). The time between each beam (different rows) was
15 minutes. The dose maps are obtained with absolute calibration using the calibration
plot obtained from the calibration samples an corrected for the discrepancy between
MSE and TSE.

425   Dose maps acquired with the TSE sequence immediately after radiation (figure 10d-

4D Radiation Dosimetry   28

f) can be compared with the TPS calculated dose map (figure 10j-l) and with dose maps

acquired by use of an MSE sequence on either the MRI-Linac (figure 10a-c) and on the

3T MRI scanner (figure 10g-i). The R_2 maps acquired with the TSE sequence were

corrected with the previously determined correction factor of 1.74 (section 3.2).

430   The higher dose resolution on the 3T MRI scanner (figure 10g) as compared to

the 1T MRI-Linac (figure 10a) can be appreciated. The field size in the longitudinal

direction (z-direction) appears to be slightly smaller in the MSE reconstructed sagittal

and coronal dose maps (figure 10b-c and h-i) as compared to the treatment planning

(figure 10k-l) which can be attributed to the relatively course slice resolution (1 cm) in

435 the MSE acquired dose maps in this direction. While a relatively good correspondence

between the different dose maps can already be observed visually, a quantitative analysis

indicated small deviations in absolute dose levels and a misalignment in the order of a

2 degree tilt of the images acquired on the 3T MRI scanner with respect to the scans

acquired on the MRI-Linac. Dose profiles in the beam directions after correction of

440 the alignment error and renormalisation of the dose towards the dose at the isocentre

are shown in figures 11a-c. A significant underdosage in the third beam can be seen

in the last dose frame acquired on the MR–Linac (figure 11c) which is attributed to

the retardation effect. It can be noted that this underestimation of dose is far less

pronounced in the MSE acquired dose map on the MRI-Linac and has completely

445 disappeared in the MSE acquired dose map on the 3T MRI scanner.

Lateral profiles through the second beam are displayed in figure 11d. Slightly

sharper penumbras are found in the MSE gel measured dose distributions as compared

to the treatment plan (table 2) and the TSE acquired dose distribution.

4D Radiation Dosimetry

29

Table 2: Penumbras for the lateral profiles in Figure 11d between 20% and 80% dose levels. The imaging pixel size is also provided.

Imaging method	Penumbra	Pixel size
MRL - MSE	3.9 mm	1mm $\times$ 1 mm
MRL - TSE	5.7 mm	1.7 mm $\times$ 1.7 mm
3T MRI - MSE	3.8 mm	1 mm $\times$ 1 mm
TPS	5.1 mm	1 mm $\times$ 1 mm

4D Radiation Dosimetry　　　　　　　　　　　　　　　　　　　　30

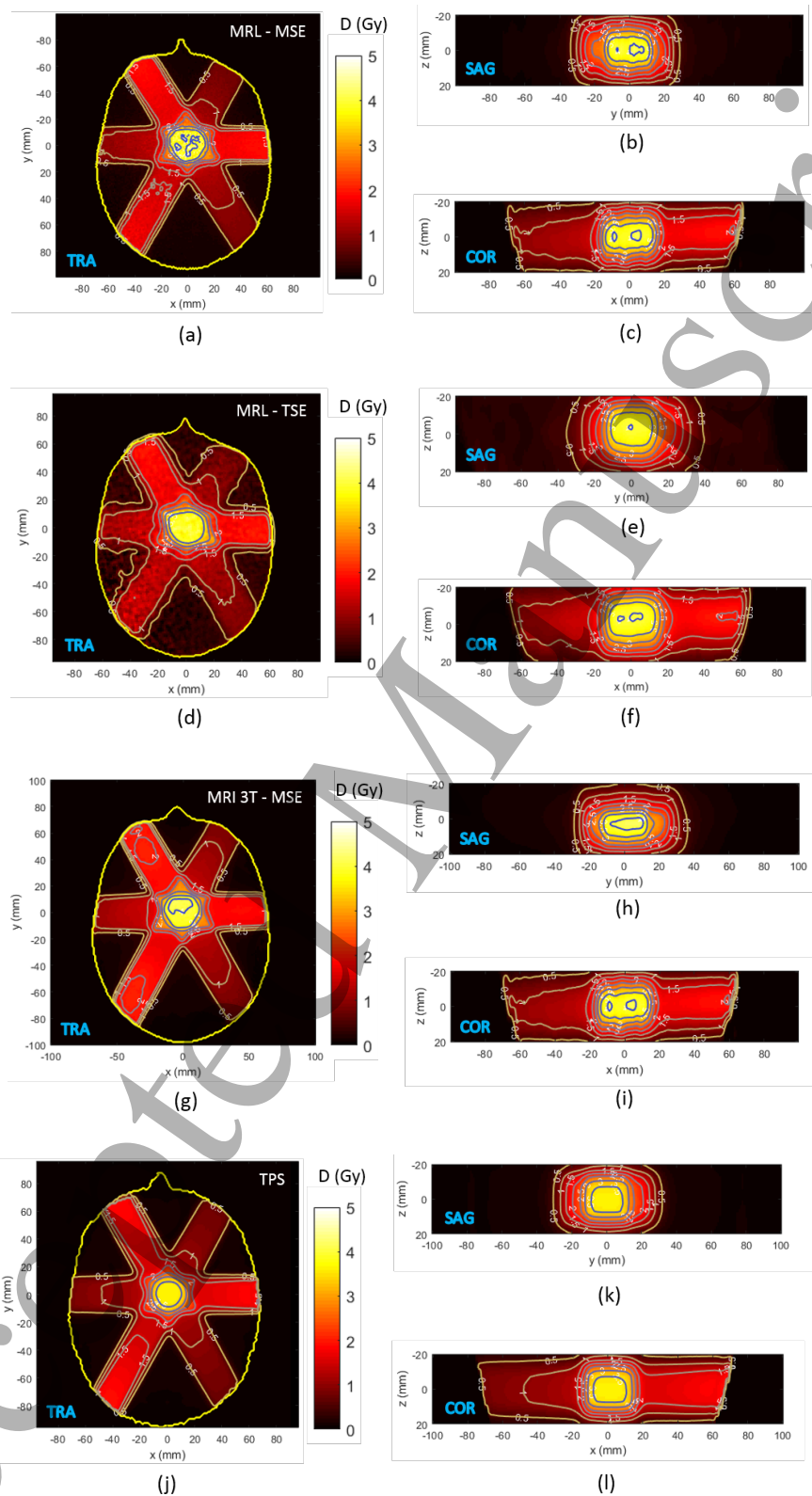Figure 10: Dose maps of the three-beam treatment of the head phantom, acquired on the MRI-Linac using the MSE scan (a-c) and using the dynamic TSE scans (d-f), acquired on the 3T MRI scanner using the MSE sequence (g-i) and calculated using the treatment planning system (j-l). Transverse maps (a,d,g,j) are acquired, while sagittal (b,e,h,k) and coronal (c,f,i,l) dose maps are reconstructed using cubic interpolation.

4D Radiation Dosimetry   31

(a)

(b)

(c)

(d)
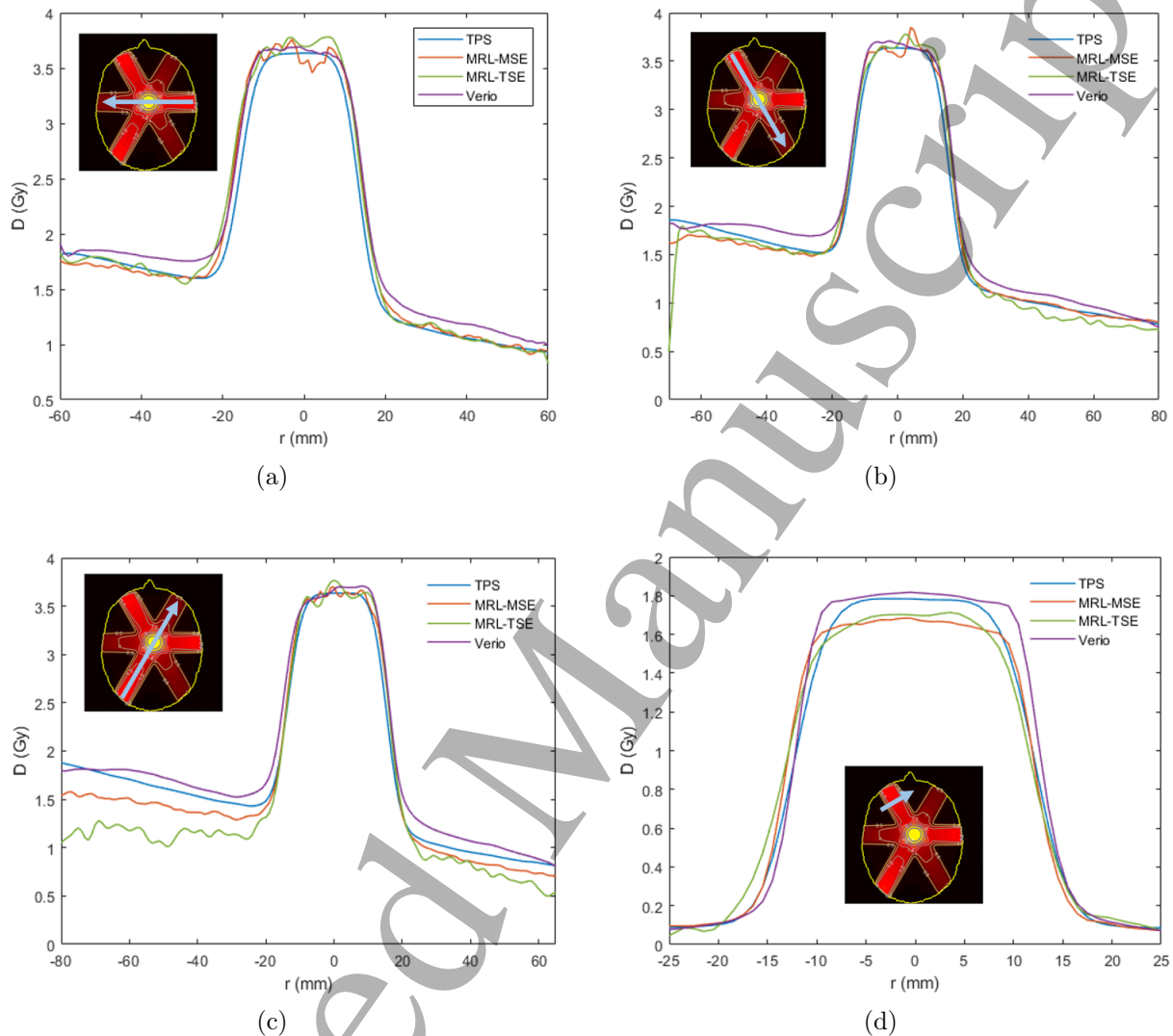
Figure 11: Dose profiles along the longitudinal direction of the radiation beams (a-c) and a lateral profile through the second beam (d) obtained with the four methods (TPS: Treatment Planning System; MRL-MSE: on the MRI-Linac using the multi-spin echo sequence; MRL-TSE: on the MRI-Linac, final frame using the Turbo-Spin-Echo sequence; Verio: on the 3T Verio MRI scanner). The dose distributions were renormalized in dose towards the dose at the isocentre. The inset figures show the direction of the dose profile.

4D Radiation Dosimetry 32

Gamma comparisons between dose maps acquired with the four different methods

450 are shown in figure 12 and corresponding gamma pass rates and dose renormalisation

coefficients are shown in table 3. The gamma pass rates are calculated in a dose region

defined by doses above 5% of the dose at isocentre. The gamma map in figure 12e

indicates that the smaller gamma pass rate of the dynamic TSE acquired dose maps is

largely attributed to the retarded dose registration of the third beam.

Table 3: Gamma pass rate for the different comparisons

Comparison	Renormalization factor	Gamma pass rate
MRL - MSE versus TPS	0.92	93.1%
MRL - TSE versus TPS	0.98	86.5%
3T MRI - MSE versus TPS	0.89	95.4%
MRL - MSE versus 3T MRI - MSE	1.04	97%

4D Radiation Dosimetry

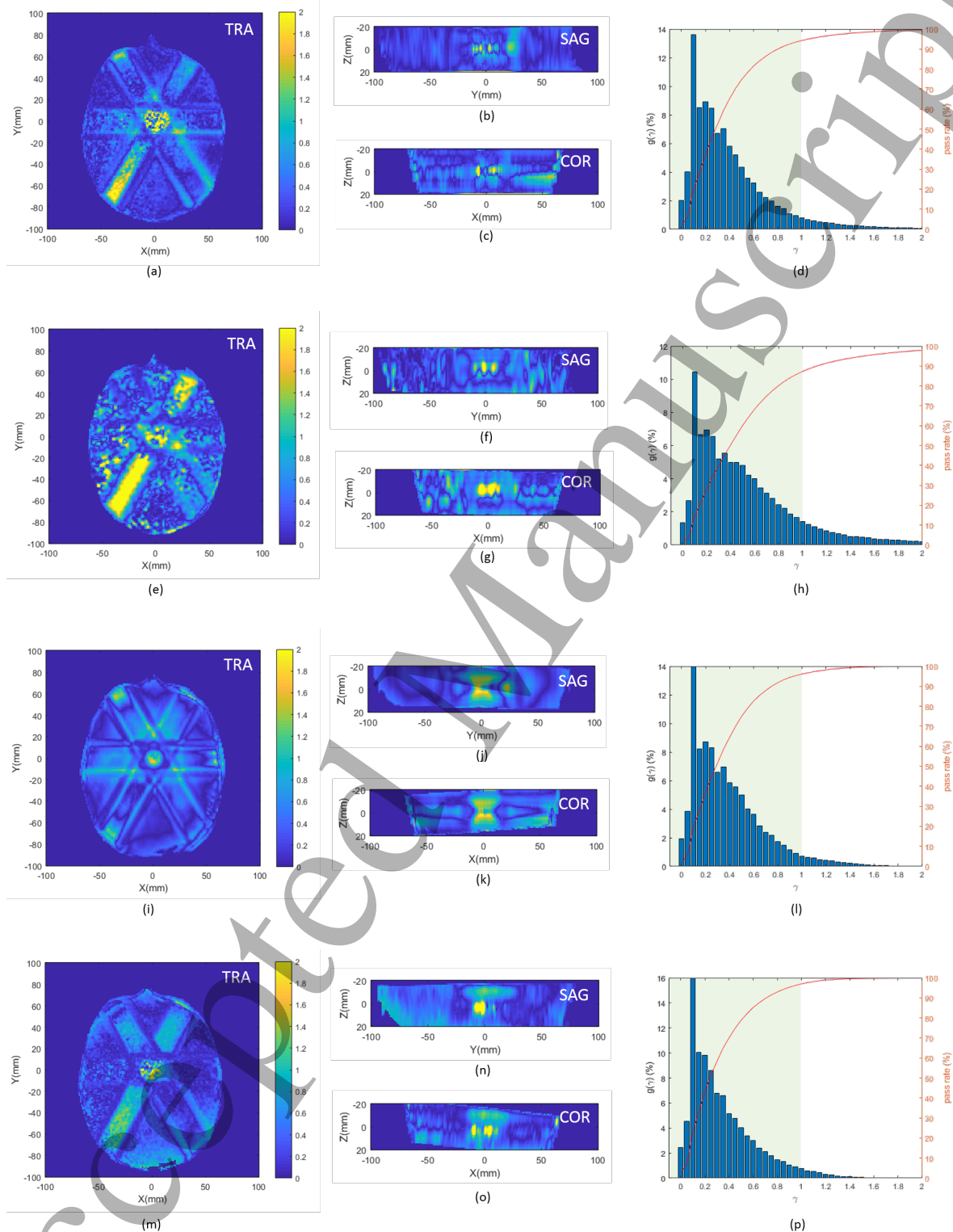Figure 12: Gamma comparisons (Dose/distance criteria = 3%/3mm): (a-d) MRL-MSE versus TPS, (e-h) MRL-TSE versus TPS, (i-l) 3T MRI - MSE versus TPS and (m-p) MRL versus Verio. Both transverse (TRA), sagittal (SAG) and coronal (COR) images through the isocentre are shown. Corresponding gamma value distributions are shown with cumulative plot (red curve) indicating the pass rate where it crosses the ($\gamma = 1$)-line.

4D Radiation Dosimetry 34

455 *3.6. 3D dose experiment: Cylinder (experiment C)*

Images acquired during the rotational delivery at different time points are shown in figure 13. A movie capture of the dose formation during treatment delivery in the five slices can be found in the Supplementary material ($\rightarrow$ MOVIE 5).
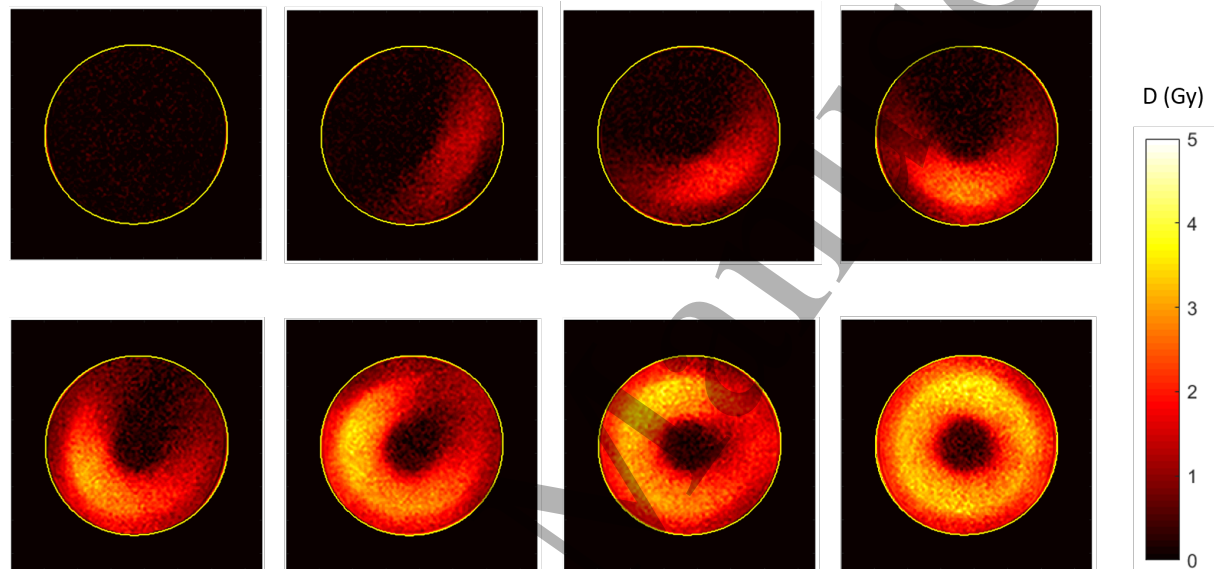
Figure 13: Dose maps recorded dynamically on the MRI-Linac during a rotational radiation delivery on a cylindrical phantom. The separation between two adjacent images is 7 recorded frames, corresponding with a time increment of 108 seconds or an angular increment of 54 degrees.

During radiation, it was observed that the dose rate of the Linac was not constant,
460 which may explain the angular variation in registered dose. To obtain a better view on the angular dose variation, the dose maps were converted to polar plots (figure 14b and f). Profiles of the angular dose variation (figure 14c and g) were obtained in an angular region between 30 mm and 40 mm from the centre of rotation as indicated by the dashed lines in figures 14a and e respectively. The high dose region is indicated
465 as the region between the two black dashed circles in figures 14a and e. Radial dose profiles were also obtained by averaging in the angular dimension (figure 14d and h).

4D Radiation Dosimetry
35
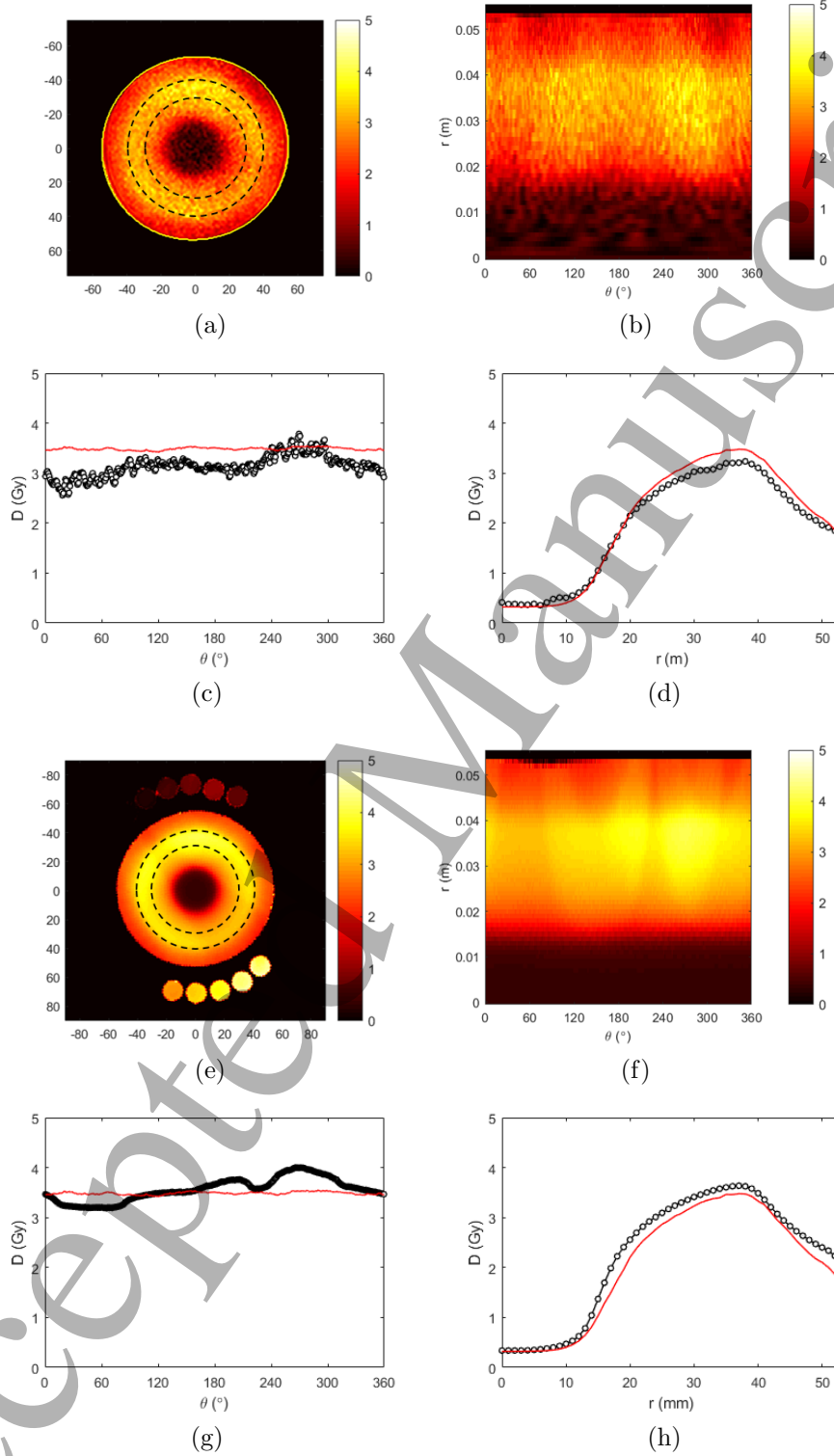
Figure 14: Dose map of the rotational radiation delivery acquired on the MRI-Linac using the dynamic TSE scan (a) with corresponding polar dose map (b). Corresponding angular dose profile in the high dose region (c) and radial profile averaged in the radial direction (d). Dose map of the cylindrical phantom and calibration vials acquired with a MSE sequence on the 3T MRI scanner (e) and corresponding polar plot (f). Corresponding angular (g) and radial profiles (h). TPS calculated profiles are shown as red solid lines. No renormalization is performed.

4D Radiation Dosimetry   36

4. Discussion

4.1. Temporal resolution and uncertainty

For quantitative measurements acquired sequentially in time, it is important to make

470   a clear distinction between 'temporal resolution' and 'temporal uncertainty'. Temporal

resolution refers to the discrete rate at which two consecutive measurements are

acquired, in other words to the 'sampling rate', while 'temporal uncertainty' refers to

the time window in which no significant signal change can be detected. Similarly, a

clear distinction needs to be made between the acquisition frame rate and the rate at

475   which a sensible dose readout can be made. We will refer to the maximum rate at which

a sensible dose readout can be obtained as the 'effective temporal resolution' and the

corresponding minimum time interval as the 'temporal uncertainty'.

The temporal uncertainty for the different studies can be calculated using the

concept of dose resolution. In radiation dosimetry, dose resolution was introduced as a

480   quantitative metric to define the minimal separation between two absorbed doses that

can be distinguished with a given level of confidence (Baldock *et al* 2001). The dose

resolution, D_Δ^p is defined as the minimum detectable dose difference within a given level

of confidence, p and is proportional to the standard deviation of dose (equation 9).

$$D_\Delta^p = k_p\sqrt{2}\sigma_D \tag{9}$$

485   where k_p is the coverage factor for the level of confidence p and σ_D is the standard

deviation on the measured dose values. For a 95% confidence level, $k_{95\%} = 1.96$ and

thus $D_\Delta^{95\%} = 2.77\sigma_D$.

A mathematical relation can be derived that relates the dose resolution D_Δ^p, the

4D Radiation Dosimetry   37

dose sensitivity of the gel and the SNR in the images (Appendix A).

$$D_{\Delta}^{p} = \frac{k_p\sqrt{2}}{\alpha TE}e^{R_{2,0}TE}\sqrt{1+e^{2\alpha DTE}}\left(\frac{\sigma_S}{S_0}\right) \tag{10}$$

where α is the R_2-dose sensitivity ($\alpha = \frac{\partial R_2}{\partial D}$), $R_{2,0}$ is the R_2 of unirradiated gel, σ_S is the amplitude of the image noise and S_0 is the signal in an image for small TE (theoretically for $TE \rightarrow 0$). The temporal uncertainty $TU_{p\%}$ can be defined as the minimum time frame in which a detectable dose difference can be detected with confidence level of $p\%$ which can be written as:

$$TU_{p\%} = \frac{D_{\Delta}^{p}}{\dot{D}} = \left(\frac{k_p\sqrt{2}}{\alpha TE\dot{D}}\right)e^{R_{2,0}TE}\sqrt{1+e^{2\alpha DTE}}\left(\frac{\sigma_S}{S_0}\right) \tag{11}$$

where $\dot{D}$ is the dose rate. As the dose resolution depends on the dose-sensitivity of the gel (α) and the dose D, the temporal uncertainty $TU_{p\%}$ is also dependent on both the type of gel dosimeter and the dose range in which dose maps are acquired. Moreover, the temporal uncertainty depends on the imaging parameter TE.

It has recently been suggested that gel dosimeters may have potential for 4D radiation dosimetry (Lee *et al* 2018, Papas *et al* 2019). However, the poor MRI dose sensitivity in both studies compromises the effective temporal resolution significantly. In the study by Lee *et al* (2018), a Fricke gel dosimeter with xylenol orange (FOX) was used. The MRI dose sensitivity of the FOX gel dosimeter is not mentioned in the paper by Lee *et al* but Fricke gel dosimeters with gelatin matrix have a typical dose-R_1 sensitivity in the order of 0.039 s^{-1}.Gy^{-1} (Audet *et al* 1997) which is further reduced by the addition of xylenol orange (Healy *et al* 2003). In the study by Papas *et al* (2019), a vinylpyrrolidone based gel dosimeter (VIPET) is used which has an R_2-dose sensitivity of 0.152 s^{-1}.Gy^{-1}.

In the paper by Lee *et al* , it is shown that the T_1-weighted signal change increases

4D Radiation Dosimetry   38

with one standard deviation in a time span of 77 seconds (which corresponds with a dose difference of approximately 7 Gy). The dose resolution with 95% confidence level $D_\Delta^{95\%}$ is 2.77 times the standard deviation. Thus, the actual detectable dose level is more than 19 Gy or the temporal uncertainty for the FOX dosimeter is 213 seconds at a dose rate of 540 cGy/min. For a courser sampling rate of 1 s, allowing 4 averages, the standard deviation is halved, which still results in a temporal uncertainty of 106 seconds.

The dose resolution for the VIPET gel dosimeter (Pappas *et al* 2019) can be calculated from equation 10. With a dose sensitivity $\alpha = 0.152s^{-1}Gy^{-1}$, an R_2 intercept $R_{2,0} = 1.411s^{-1}$, a noise ratio $\sigma_S/S_0 = SNR^{-1} = 0.033$ and an echo time $TE = 500ms$ the dose resolution $D_\Delta^{95\%}$ varies between 2.46 Gy and 4.36 Gy for a dose range between 0 Gy and 4 Gy. Assuming a similar dose rate of 540 cGy/min, the corresponding temporal uncertainty ranges between 27 s and 48 s. The signal-to-noise ratio was not mentioned in the paper by Pappas *et al* (2019) nor was the number of slices and the slice thickness. Because the previous study was conducted on a 1.5 T MRI-Linac (Elekta Unity), a 50% higher SNR was considered than what we achieved on the 1 T MRI Linac.

The dose resolution for the MAGAT gel dosimeter applied in our study on the Australian MRI-Linac ranged from 0.35 Gy to 2.4 Gy for a dose range between 0 Gy and 4 Gy, which corresponds with temporal uncertainty of 21 seconds at a dose rate of 100 cGy/min or 3.8 seconds at a dose rate of 540 cGy/min. It can be noted that for a similar dose rate as the previous studies and on a 1.5 T Unity, the temporal uncertainty reduces theoretically to 2.5 seconds (Table 4).

To illustrate the concept of effective temporal resolution (temporal uncertainty) and its relation to dose resolution, a hypothetical case can be considered where a single

4D Radiation Dosimetry　　　　　　　　　　　　　　　　　　　　　39

Table 4: Overview of temporal uncertainties of previous MRI-Linac gel dosimetry studies and this study.

Study	Temporal uncertainty $TU_{95\%}$
Lee *et al* 2018	106 seconds
Pappas *et al* 2019	27 seconds
This study (on a 1 T MRI-Linac)	3.8 seconds
This study (on a 1.5 T MRI-Linac)	2.5 seconds

pixel is considered to receive radiation while neighbouring pixels are not irradiated (figure 15). In figure 15, every column corresponds with a recorded dose frame. In the conversion from R_1 or R_2 to absorbed radiation dose, noise in the R_1 or R_2 maps will be converted to noise in the dose maps (with standard deviation σ_D). It can be noted

540　that the noise in the dose maps will be inversely proportional to the sensitivity of the dosimeter. Random noise is superimposed in correspondence to the standard deviation in dose for the corresponding gel dosimeter. The point in time where a pixel receiving radiation can be distinguished from unexposed pixels with 95% certainty (i.e. $TU_{95\%}$) is indicated by an arrow. For the FOX gel dosimeter, $TU_{95\%}$ is outside of the displayed

545　time scale.

4D Radiation Dosimetry   40
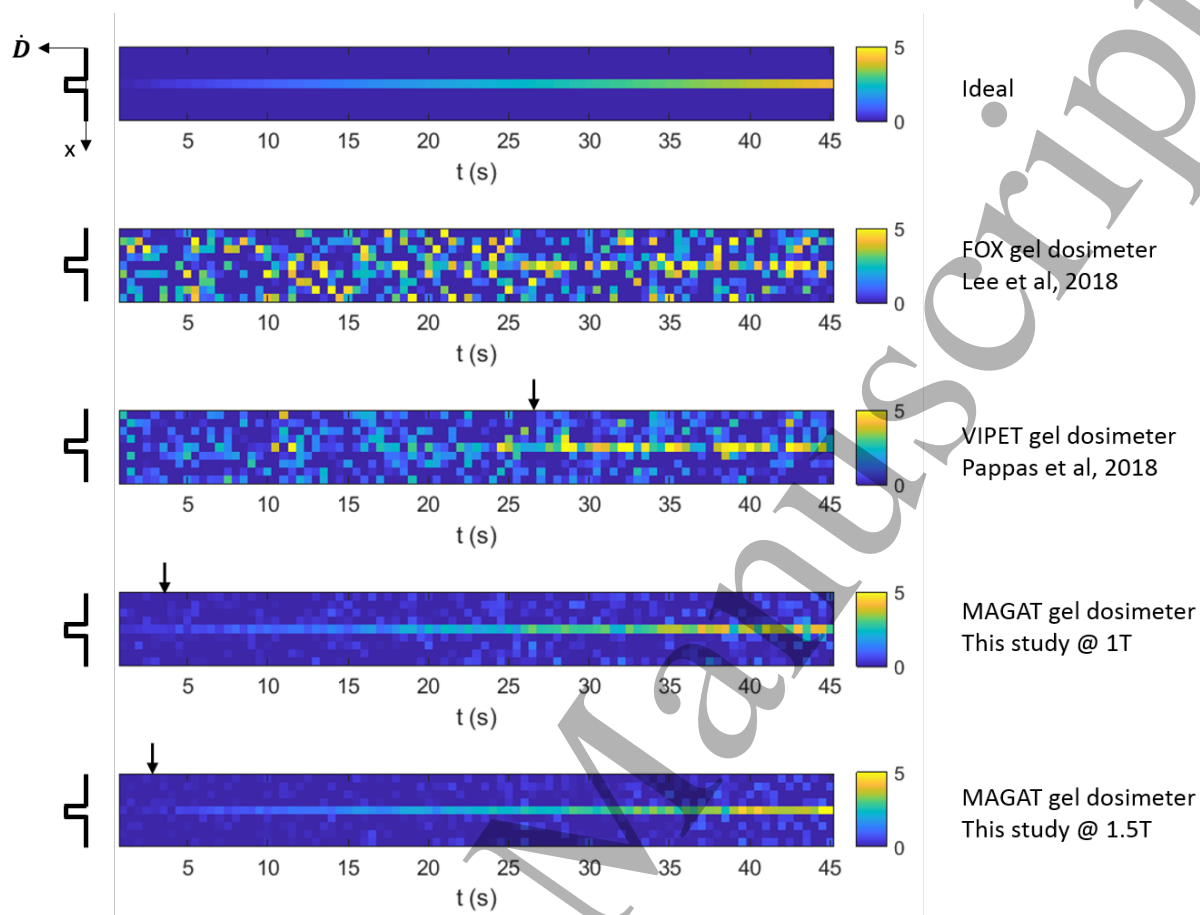
Figure 15: Hypothetical dose profiles of a single pixel receiving radiation (at a dose rate of 540 cGy/min) while neighbouring pixels remain unirradiated for different proposed gel dosimeters. The arrow indicates the temporal uncertainty $TU_{95\%}$. For the FOX gel dosimeter, the temporal uncertainty is at 106 s.

4.2. Dosimetric properties of the MAGAT gel dosimeter

In comparison to other gel dosimeters, the MAGAT gel dosimeter demonstrates a very high dose-R_2 sensitivity in the order of 4.2 - 4.5 $s^{-1} \cdot Gy^{-1}$. The high sensitivity of MAGAT gel dosimeters (De Deene *et al* 2006a) is related to a high chemical conversion rate of monomer in combination with the efficient fast magnetization exchange between hydrogen protons from hydroxyl-groups on the polymer and hydrogen protons from the water pool (Lepage *et al* 2001a). It is worth mentioning that chemical consistency is important in obtaining gel dosimeters with consistent dose-R_2 sensitivities. During this

4D Radiation Dosimetry   41

research, we noticed that the batch of anti-oxidant (THP) had a significant influence on

555   the dose-R_2 sensitivity. This may also explain that a higher dose-R_2 sensitivity is found

in this study as compared to a previous study (De Deene *et al* 2006a).

No thorough interbatch reproducibility study has been performed for the MAGAT

gel dosimeter yet, as was conducted for the PAGAT gel dosimeter (Vandecasteele and

De Deene 2013). However, figure 3 showing the dose-R_2 plots for the 4 experiments, is

560   indicative of a relatively good inter-batch reproducibility. No active temperature control

on the gel dosimeters was performed and technical problems with the air-conditioning

may have resulted in a temperature uncertainty in the order of 2 degrees Celsius.

However, from figures 3a and c, it can be seen that the dose-R_2 response plots of the

different experiments follow similar trends on the MRI-Linac and the 3T MRI scanner,

565   which suggests that the difference in dose-R_2 response in the various experiments is

most likely related to variations related to the fabrication process.

Compared to many other gel dosimeters, the dose-R_2 response of the MAGAT gel

dosimeter has a very good temporal stability (De Deene *et al* 2006a). This superior

temporal stability can be attributed to the fact that the methacrylic acid polymer

570   grafts onto the gelatin matrix in contrast to other vinyl or acrylic based polymer gel

dosimeters where the polymer aggregates precipitate inside the gel matrix (De Deene

et al 2000c, Fuxman *et al* 2005, Kozicki 2011) or to Fricke gel dosimeters where the

ferrous and ferric ions diffuse through the gel matrix. We postulate that the grafting

of linear methacrylic acid polymer onto gelatin is also responsible for a relatively fast

575   chemical reaction in contrast to a significant relative change in R_2-dose sensitivity in

PAG gel dosimeters in the first 10 hours post-radiation. Despite the relatively fast

response, some post-radiation response is still noticeable (figure 4) immediately after

4D Radiation Dosimetry   42

radiation. The gel measured dose as a function of time t during and after radiation can be well described by a first order retarded response as discussed in appendix B. The

580   time constant of the retarded response is expected to depend on the reaction kinetics of radiation-induced polymerization and the structural formation of the polymer network. As the methacrylic acid polymer grafts onto the gelatin matrix in the MAGAT gel dosimeter, it can be expected that the gel matrix will have an influence on the response time. This post-radiation response is important to keep in mind for the quantitative

585   interpretation of real-time registered dynamic dose maps as illustrated in experiments A and C.

The MAGAT gel dosimeter has a dose rate dependence similar to other polymer gel dosimeters and negligible energy dependence (De Deene *et al* 2006a). The R_2-dose response of the MAGAT gel dosimeter is dependent on the temperature during radiation

590   and during scanning. The change in R_2 per degree Celsius during scanning ranges from $0.08 \ s^{-1}(^{\circ}C)^{-1}$ to $0.344 \ s^{-1}(^{\circ}C)^{-1}$ in the dose range of 0 Gy to 4 Gy (De Deene *et al* 2006a). The corresponding dose uncertainty for a temperature uncertainty of $1^{\circ}C$ between calibration and dosimeter phantom is 0.036 Gy for an unirradiated sample (0 Gy) and 0.16 Gy for a sample irradiated to 4 Gy, which corresponds to a dose uncertainty

595   ranging from 1% to 4% of the maximum dose. The dose error induced by a temperature difference of $1^{\circ}C$ during radiation as a result of a temperature dependent response of the radio-chemical reaction amounts to 2%. It can be noted that both temperature-induced errors work in the same direction. Therefore, a temperature uncertainty of $1^{\circ}C$ during both radiation and scanning is expected to result in an absolute dose uncertainty of

600   6%. For an extreme temperature variation of $2^{\circ}C$ this would result in an absolute dose uncertainty of 12%.

The MAGAT gel dosimeter is found tissue equivalent with a total mass attenuation coefficient relative to water between 1 and 1.045 in the energy range 10 keV - 100 MeV (De Deene *et al* 2006a), which results in a CT number for the MAGAT gel of 40 HU.

605   It has previously been shown that a low-density MAGAT gel dosimeter can be created by beating the gel to a gel foam which was found to have a microstructure similar to lung parenchyma (De Deene *et al* 2006b). The low-density MAGAT gel dosimeter can not be read out with quantitative R_2 imaging but it can be read out by use of quantitative magnetization transfer, while quantitative R_2 dispersion measurements

610   can be used to assess the foam microstructure (Baete *et al* 2008).

A concern with PAGAT polymer gel dosimeters has been that the dose-R_2 response would be dependent on the size of the gel phantom and as a result induces uncertainties while using a calibration with small calibration vials (De Deene and Vandecasteele 2013a, 2013b). Several studies have been conducted to find the reasons for the difference in

615   the dose-R_2 response such as a difference in cooling temperature after pouring the gel in recipients (De Deene *et al* 2007), temperature changes during radiation as a result of exothermal polymerization (Salomons *et al* 2002), oxygen diffusion (Sedaghat *et al* 2010) and magnetic susceptibility artefacts (De Deene and Vandecasteele 2013b). An experiment whereby a small test tube filled with MAGAT gel was inserted in a larger

620   spherical phantom with MAGAT gel of the same batch shows that no difference in dose-ΔR_2 response is visible on the MRI-Linac. In high resolution MSE derived R_2 maps acquired on the 3T MRI scanner, an increase in R_2 is detected in a region of 1 mm near the glass wall. The small increase in R_2 near the glass wall does not impact the accuracy of the calibration as R_2 values are extracted from a central ROI which is at

625   least 2 mm away from the glass wall.

4D Radiation Dosimetry   44

4.3. MRI acquisition

A TSE sequence was used to acquire dynamic dose maps because of its relatively low
sensitivity to magnetic field inhomogeneity and minimal image distortions as compared
to gradient echo-based pulse sequences. The optimal echo time in the TSE sequence
630 is dependent on the dose, varying from 500 ms at 0 Gy to 60 ms at 4 Gy (figure A1).
In optimizing the imaging protocol, it is also important to consider the sampling rate
in relation to the spatial resolution, the receive bandwidth and turbo factor. For both
MSE and TSE acquired dose maps, the temporal uncertainty and dose resolution are
inversely proportional to the SNR in the base images. A significant difference in dose
635 resolution can be seen between the dose distributions in experiment A (figure 7) and
experiment C (figure 10), which illustrates the importance of sequence optimization.
The single beam experiment (A) was not optimized with respect to the higher doses
($TE = 272\ ms$), had a relatively high spatial resolution, a repetition time of 2 s and
a bandwidth of 275 ms, resulting in a SNR of 9.15 in the TSE images, while the time
640 interval between two frames was 48 s. The echo time in the TSE sequence for the
three-beam treatment on the head phantom (experiment C) was optimized for a dose
of 1 Gy ($TE = 160\ ms$). To decrease the measurement time in the latter experiment,
a repetition time of 1 s was chosen and the matrix size was reduced from $256{\times}256$ to
$128{\times}128$, resulting in an imaging frame rate of 11 s. Five slices with a slice thickness of
645 1 cm were recorded. The SNR in the TSE images for the three-beam experiment was
24, an increase in SNR with a factor of 2.6.

The maximum dose rate that can be achieved with the Australian MRI Linac in
the phantoms was approximately 1 Gy/min. The maximum dose increment in one

4D Radiation Dosimetry   45

frame of 18 seconds is 30 cGy, which is in the same order of magnitude as the dose

650 resolution. A faster frame rate would be below the detection limit and therefore

useless. For MRI-Linac systems that can achieve higher dose rates, higher frame

rates may be required. This can be achieved by faster imaging pulse sequences and

compressed sensing. Paramount in the selection of fast imaging approaches is a unique

correspondence between signal intensity and radiation dose and a high spatial fidelity.

655 Because of the specific spatial information content in radiation dose distributions, it can

be expected that only specific parts in the k-space will contain essential information. It

can thus be expected that dynamic scanning of MRI dose maps would largely benefit

from a keyhole approach, as for example applied in dynamic contrast enhanced (DCE)

MRI.

660   A deviation between ΔR_2 acquired with a TSE sequence and ΔR_2 acquired with an

MSE sequence is observed. On the 3T MRI scanner, the deviation can be explained by

an incomplete and dose dependent longitudinal magnetization recovery. On the MRI-

Linac, the deviation is significantly larger which is attributed to an imperfection in the

RF pulses. It was found that the turbo factor in the TSE sequence had no significant

665 effect on the ΔR_2 values, however it is important to note that high turbo factors result in

a broadening of the point spread function and may thus compromise the intrinsic spatial

resolution. It was found that the RF pulse amplitudes on the experimental 1T MRI-

Linac were insufficient to cause full excitation and refocussing. The effect of non-ideal

RF pulses has been discussed in appendix C. While the large discrepancy in transmit

670 voltages may be a specific problem with the experimental MRI-Linac, the description

is more generally applicable to estimate the dose uncertainty as a result of imperfect

B_1-field, for example in larger size dosimeters, such as 3D pelvic dosimeters (Vergote

4D Radiation Dosimetry   46

et al 2004). Experiments on the 3T MRI scanner and Bloch simulations demonstrate

that a 20% heterogeneity in B_1 around the ideal B_1 results in a dose uncertainty of only

675 1.2% for the TSE sequence and 3.6% for the MSE sequence with imaging parameters as

used in this study. For a 30% deviation in B_1 from the ideal value, the dose uncertainty

increases rapidly to 6% for the TSE sequence and 8% for the MSE sequence. It can be

concluded that if the B_1-field heterogeneity exceeds 20% of the optimum value, a B_1-

field compensation is required, following methods described in the scientific literature

680 (De Deene *et al* 2000b, Lepage *et al* 2001b, Vergote *et al* 2004). It is important to note

that the relation between B_1-field amplitudes (or transmit voltage amplitudes) and

the deviation in ΔR_2 depend on the pulse sequence and thus may be site dependent.

Therefore, any implementation of B_1-field heterogeneity compensation strategy needs

to be developed on the basis of the pulse sequence used.

685 *4.4. Clinical dose verification*

For both the three-beam radiation and the dynamic rotational treatment, a relatively

good agreement is found between the dose distributions obtained on the MRI-Linac, on

the 3T MRI scanner and TPS calculated dose distributions. However, for the three-

beam treatment, a systematic higher dose of approximately 8% and 11% is registered

690 in the MSE acquired dose distributions on the MRI-Linac and the 3T MRI scanner

respectively. For the three-beam treatment, gamma pass rates between MSE acquired

dose distributions and TPS calculated dose distributes are above 93% for gamma criteria

of 3%/3 mm after normalisation towards the dose at the isocentre. A lower pass rate of

86% is found for the TSE acquired dose distribution compared to the TPS calculated

695 dose distribution. The lower gamma pass rate is attributed to a cluster of high gamma

4D Radiation Dosimetry   47

values at the location of the third (last) beam (figure 12e). The large deviation in the third beam is the result of an ongoing post-irradiation polymerization leading to an underdeveloped registered dose of the third beam, as can also be seen from the profiles in figure 11c. Indeed, the MSE acquired dose profile acquired immediately after the dynamic TSE scanning already shows an increase in registered dose, and the MSE acquired dose distribution acquired on the 3T MRI scanner, acquired approximately12 hours after radiation, shows a fully developed dose profile.

700

Slightly sharper penumbras are found in the MSE acquired dose maps than in the dynamic TSE acquired dose maps and the TPS calculated dose maps, with the shallowest penumbras in the TSE acquired dose maps (table 2). The more shallow penumbras in the TSE dose maps may be partially attributed to the lower spatial resolution in the TSE scans (1.7 mm as compared to 1 mm) and the line broadening as a result of the T_2-weighting of k-space lines within the same echo train.

705

As a result of dose rate variations during the rotational treatment, angular variations in the dose distribution are visible, however, the angular averaged radial dose distributions (figure 14d and h) show a relatively close agreement with the TPS calculated dose distribution. In comparison to the TPS calculated dose distribution, the dynamic TSE acquired dose distribution is approximately 7% lower while the MSE acquired dose distribution is approximately 4% higher. Also in this experiment are MSE acquired dose values on the 3T MRI scanner higher than the TSE acquired dose values on the MRI-Linac, possibly as a result of the ongoing post-radiation polymerization.

710

715

It is worth mentioning that during some other experiments (results not shown), non-intentional misalignment errors were observed where the dynamic dose information proved helpful in tracing the source of the deviations.

4D Radiation Dosimetry 48

720 5. Conclusions

The feasibility of 4D radiation dosimetry on an MRI-Linac by use of a high sensitivity polymer gel dosimeter has been demonstrated in cylindrical and humanoid shaped phantoms. Dynamic ΔR_2 maps are acquired by use of a TSE sequence which can be converted in dose maps by use of an MSE acquired dose-ΔR_2 calibration plot. To
725 use the MSE acquired dose-ΔR_2 calibration plot, a correction factor needs to be applied that accounts for incomplete longitudinal relaxation recovery and non-ideal RF pulses.

The effective temporal resolution depends on the optimal dose resolution that can be achieved with a particular gel dosimeter and with a dynamic MRI pulse sequence. The MAGAT gel dosimeter has a dose-R_2 sensitivity of 4.5 $s^{-1}.Gy^{-1}$. Optimal echo
730 times have been derived to minimize the dose resolution calculated from the dynamic TSE scans.

The concept of temporal uncertainty $TU_{95\%}$ is introduced to describe the effective temporal resolution that is achievable with a particular 3D gel dosimeter. For the MAGAT gel dosimeter, the temporal uncertainty at a dose rate of 540 cGy/min and in
735 a magnetic field of 1 Tesla is 3.8 s, which is at least an order of magnitude smaller than in previously suggested 4D dosimeters. While the current MAGAT gel dosimeter has a superior stability above other polymer gel dosimeters, a retardation in dose response has been detected with a characteristic time of 83 s. This retarded response is related to the radiation chemistry kinetics of the monomer and the gel matrix and is thus also
740 related to the gel dosimeter composition. It has been demonstrated that the retarded response compromises the accuracy of the dynamically TSE acquired dose maps in a clinical dose validation study.

4D Radiation Dosimetry   49

While progress has been made with this study towards 4D dosimetry with an increase in effective temporal resolution and with a reasonable correspondence with TPS calculated dose distributions (with gamma pass rate 86%), it is the authors' opinion that the main application of the dosimeter at its current stage is for assessing beam misalignments during treatment. The good correspondence of the final acquired dose distribution with the TPS calculated dose distribution (with a gamma pass rate above 95%), adds evidence to previous studies on the usefulness as relative 3D dosimeter.

Future studies are required to find a more optimal gel formulation with reduced retardation and temperature dependence. Future research will also focus on improving the dose resolution and temporal resolution by use of a keyhole imaging approach. In the development of quantitative MR imaging methods for real time 3D radiation dosimetry it is important to remain vigilant of MRI induced image distortions as a result of magnetic field and gradient non-uniformity and magnetic susceptibility differences.

4D Radiation Dosimetry   50

Appendix A - Optimal echo time for dynamic scanning

A mathematical relation between dose resolution and the echo time spacing in MSE sequences is provided elsewhere (De Deene *et al* 1998, 2002).

760   In this appendix, a derivation of the relation between dose resolution and echo time, extracted from two T_2-weighted images is given. In the described experiments the two images correspond to a TSE image acquired before radiation ($D = 0\ Gy$) and an image acquired at time t, where each pixel in the image has received a dose $D(x, y, z, t)$. For convenience, in the remainder of this derivation, we will leave out the spatial coordinates and time stamp and will refer to the dose in one corresponding pixel and at a certain

765   time as D.

The relation between signal intensity in the T_2-weighted image acquired with an effective echo time TE and sufficiently long repetition time is given by equation A.1

$$S = S_0 e^{-R_2 \cdot TE} \tag{A.1}$$

Assuming a linear relation for the R_2 - dose response, $R_2 = \alpha D + R_{2,0}$, the signal

770   intensity in a pixel of both TSE images can be written as

$$S(0) = S_0 e^{-R_{2,0} \cdot TE} \tag{A.2}$$

$$S(D) = S_0 e^{-R_2 TE} = S_0 e^{-(R_{2,0} TE + \alpha D TE)} = S_0 e^{-R_{2,0} \cdot TE} e^{-\alpha D TE} \tag{A.3}$$

where $S(0)$ is the signal intensity in a pixel of a TSE image acquired before radiation and $S(D)$ is the signal intensity in a pixel of a TSE image acquired at a time t during radiation.

The ratio of both signal intensities is then

775     $$\frac{S(0)}{S(D)} = e^{\alpha D TE} \tag{A.4}$$

4D Radiation Dosimetry 51

Solving for the dose D results in the straightforward expression

$$D = \frac{1}{\alpha TE} \, ln \left(\frac{S(0)}{S(D)} \right) \tag{A.5}$$

Assuming Gaussian noise in the TSE images with standard deviation σ_S, the standard

deviation on the calculated dose D, σ_D can be written as

$$\sigma_D = \frac{1}{\alpha TE} \sqrt{ \left(\frac{\partial ln \left(\frac{S(0)}{S(D)} \right)}{\partial S(D)} \right)^2 \sigma_S^2 + \left(\frac{\partial ln \left(\frac{S(0)}{S(D)} \right)}{\partial S(0)} \right)^2 \sigma_S^2 } \tag{A.6}$$

By substituting equation A.4 into equation A.6, the standard deviation σ_D, is given by

$$\sigma_D = \frac{1}{\alpha TE} e^{R_{2,0}TE} \sqrt{1 + e^{2\alpha DTE}} \left(\frac{\sigma_S}{S_0} \right) \tag{A.7}$$

The optimum echo time, TE_{opt} for a given dose, D can be calculated from

$$\frac{\partial \sigma_D}{\partial TE} = 0 \tag{A.8}$$

which results in the transcendental equation

$$\left(\frac{1 - R_{2,0}TE}{\alpha DTE - 1 + R_{2,0}TE} \right) = e^{2\alpha DTE} \tag{A.9}$$

Note that the same values for TE_{opt} are found for the relative dose uncertainty, $\frac{\sigma_D}{D}$. The

roots of the transcendental equation can be calculated by use of a numerical root-finding

algorithm. The results of the optimization analysis (using Matlab®) are provided in

figure A1.

4D Radiation Dosimetry
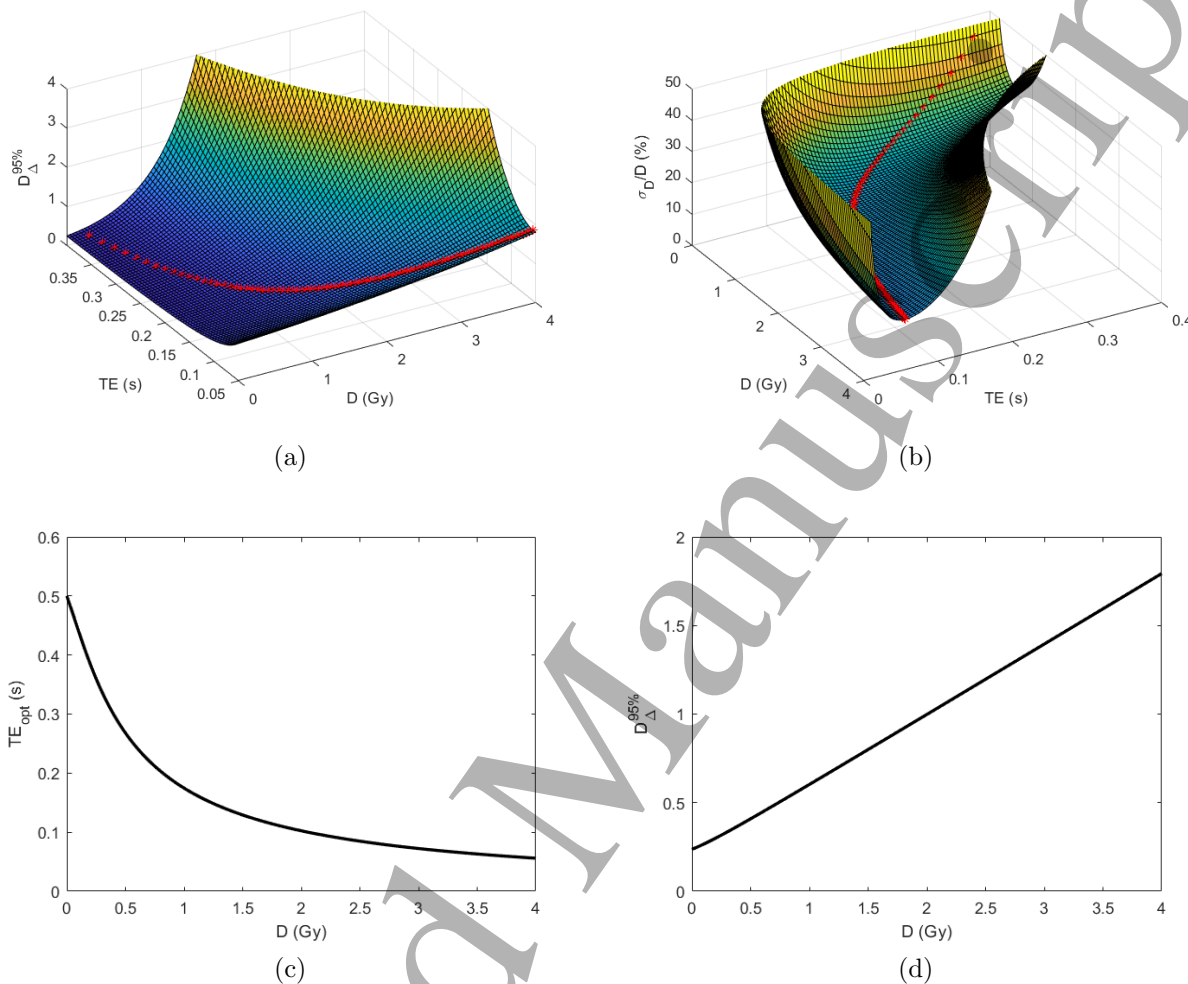
52

(a)

(b)

(c)

(d)

Figure A1: Dose resolution for different doses and echo times for the MAGAT gel dosimeter (a) and corresponding relative dose error (b). A noise level of 5% (SNR = 20) is assumed in these calculations. Values for optimal echo times are indicated as red symbols in both 3D plots. The optimum echo time and corresponding dose resolution are plotted in (c) and (d) respectively.

Appendix B. Retarded Response Function

Some ongoing dose response was found after the radiation beam was switched off. To model this retarded response, for simplicity, we assume a first order kinetic response on radiation delivery. Here, a saturating exponential function applies to the response to

4D Radiation Dosimetry   53

795 any infinitesimal amount of absorbed dose which can be written mathematically as

$$\Delta D_r = \dot{D}\Delta t(1 - e^{-t/\tau_r}) \tag{B.1}$$

where ΔD_r is the MRI registered dose, $\dot{D}$ is the dose rate, t is the time after delivery of an infinitesimal amount of dose and τ_r is the time constant for the retarded reaction.

Taking the limit for the time increment toward zero results in a first order linear 800 differential equation for the response during radiation delivery ('beam on').

$$\frac{dD_r}{dt} = \dot{D}(1 - e^{-t/\tau_r}) \tag{B.2}$$

and thus

$$D_r(t) = \int_0^t \dot{D}(1 - e^{-\tau/\tau_r})d\tau = \dot{D}t + \dot{D}\tau_r(e^{-t/\tau_r} - 1) \tag{B.3}$$

which results in

805 $$D_r(t) = \dot{D}t + \dot{D}\tau_r(e^{-t/\tau_r} - 1) \qquad \text{for } 0 \leq t \leq t_{rad} \tag{B.4}$$

When the radiation is switched off, the registered dose is still accumulating as a result of the retarded response of each of the small absorbed dose increments during radiation delivery.

$$D_r(t) = \sum_{i=1}^{N_{rad}} \dot{D}\Delta t(1 - e^{-(t-i\Delta t)/\tau_r}) \tag{B.5}$$

$$= \dot{D}\Delta t\left(N_{rad} - e^{-t/\tau_r}\sum_{i=1}^{N_{rad}} e^{i\Delta t/\tau_r}\right) \tag{B.6}$$

where N_{rad} is the number of absorbed dose increments and D is the total absorbed dose 810 after total delivery. Note that $N_{rad}\cdot\Delta D = \dot{D}\cdot\Delta t = D$. If we consider infinitesimal dose increments ($\Delta t \to 0$, $N_{rad} \to \infty$), equation B.6 can be expressed as an integral equation

$$D_r(t) = D - \dot{D}e^{-t/\tau_r}\int_0^{t_{rad}} e^{\tau/\tau_r}d\tau \tag{B.7}$$

which results in

$$D_r(t) = D - \dot{D}\tau_r e^{-t/\tau_r}(e^{t_{rad}/\tau_r} - 1) \qquad \text{for } t \geq t_{rad} \tag{B.8}$$

4D Radiation Dosimetry   54

815 where t_{rad} is the duration of the radiation.

Appendix C. Influence of non-ideal RF pulses on measured R_2

Non-ideal excitation and refocussing pulses as a result of non-optimal transmit voltages
may result in different R_2 values. To investigate the effect of non-ideal RF pulses
on the acquired R_2 values, we performed simulations using a numerical solution of
820 the generalised Bloch equations (De Deene *et al* 2000b, Benoit-Cattin *et al* 2005,
Xanthis *et al* 2014). The simulation software was developed in house in Matlab®.

In these simulations, 128 x 128 x
128 isochromats are considered that are
uniformly distributed in a rectangular
825 voxel with dimensions 1.5 mm × 1.5
mm × 15 mm and the pulse sequence
is discretised in small time steps of 10
μs. To account for line broadening
within the voxel, a random distribution
830 of magnetic field deviation that follows
a Cauchy-Lorentz distribution is used
for the magnetic field distribution of
isochromats (figure C1).

Figure C1: Distribution of magnetic field
deviations corresponding with a T2* = 50
ms inside a voxel containing $128 \times 128 \times 128$
isochromats.

The RF pulse scheme in the TSE sequence follows a CPMG sequence $90_x - 180_y -$
835 $[180_y]_{n-1}$ where n is the number of echoes and subscripts x and y correspond with the
axis around which the magnetization is rotated with this corresponding nutation angle.
The link between the flip angle and transmit voltage is not linear as it depends on the
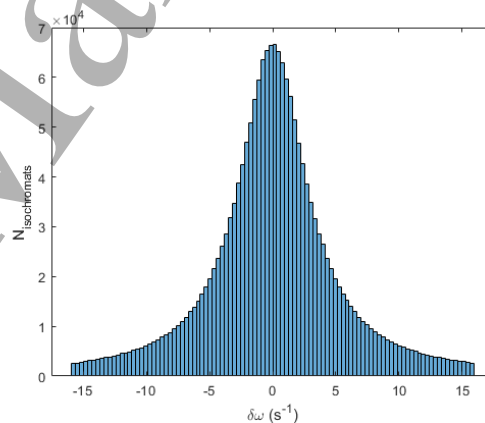
4D Radiation Dosimetry   55

RF pulse shape and duration of the RF pulses. For the TSE sequence implemented on

the MRI-Linac the ratio between the voltage of ideal refocussing pulses and excitation

840   pulse is 1.59.

For each time step, the effect of the magnetic field gradients and RF pulses on

the magnetization vector is calculated by the application of corresponding rotation

operations on each isochromat. The magnetization at an incremental point in time

$\vec{M}(\vec{r}, t + \Delta t)$ for an isochromat at position $\vec{r}$ can be described by the transformation:

$$\vec{M}(\vec{r}, t + \Delta t) = \boldsymbol{R_z}(\theta) \cdot \boldsymbol{R_{RF}} \cdot (\boldsymbol{E}(R_1, R_2) \cdot \vec{M}(\vec{r}, t) + \vec{E}_1) \tag{C.1}$$

where $\boldsymbol{E}(R_1, R_2)$ and $\vec{E}_1$ are (3×3) and (3×1) matrices accounting for longitudinal

and transverse relaxation, $\boldsymbol{R_{RF}}$ a (3×3) rotation matrix for the rotation along an axis

in the transverse plane defined by the B_1 field and $\boldsymbol{R_z}(\theta)$ is a (3×3) rotation matrix

around the z-axis which incorporates the magnetic field at position $\vec{r}$ as a result of slice

850   selective gradients, frequency encoding gradients and random magnetic field deviations

(line broadening).

Similar gradient shapes and RF pulse shapes as in the TSE pulse sequence are

used. The amplitudes of the RF pulses were chosen on the basis of the transmit

voltages that were applied, and simulations were performed for different R_1 and R_2

855   values corresponding with MAGAT gel irradiated to different dose levels. The signal

intensity was calculated as the bulk transverse magnetization at the moment of each

echo (ADC). A typical Bloch simulation is illustrated in figure C2 showing the pulse

sequence and the evolution of the total nuclear bulk magnetization in a voxel.

Bloch simulations were conducted for different scenarios: with perfect RF pulses

860   (i.e. $90_x - 180_y - [180_y]_{n-1}$) and for scenarios where the RF pulses deviate as a

4D Radiation Dosimetry   56

Figure C2: Sequence diagram of the Bloch simulation on a voxel with $128 \times 128 \times 128$ isochromats. The isochromat distribution corresponds with a T2* = 50 ms. From top to bottom are displayed: the RF pulse B_1-field, the time of acquisition (ADC), the gradient in the frequency encoding direction (G_{freq}) and corresponding gradient moment (μ_{freq}), the slice selection gradient (G_{sl}) and corresponding gradient moment (μ_{sl}) and magnetization components (M_x, M_y, M_z).

result of a limitation of the maximum transmit voltage. For each set of RF-pulses, the magnetization as a function of echo time was simulated for different R_1 and R_2 values. The R_1 and R_2 were correlated on the basis of the independent measurements on the irradiated samples discussed in section 3.2. To validate the Bloch simulations, experiments were conducted on the 3 T MRI scanner where the transmit voltages could be varied. While the ratio in transmit voltages between excitation and refocussing pulses could not be varied on the MRI scanner, the results indicate that the Bloch simulations provide realistic results. Figure C3a shows ΔR_2-dose response curves acquired on the 3 T MRI scanner and simulated using the Bloch simulator. The effect of a deviation in

1
2
3
4
5
6
7
8
9
10
11
12
13
14
15
16
17
18
19
20
21
22
23
24
25
26
27
28
29
30
31
32
33
34
35
36
37
38
39
40
41
42
43
44
45
46
47
48
49
50
51
52
53
54
55
56
57
58
59
60

4D Radiation Dosimetry 57

870 the transmit voltage on the acquired ΔR_2 is clearly visible in both the experiments and
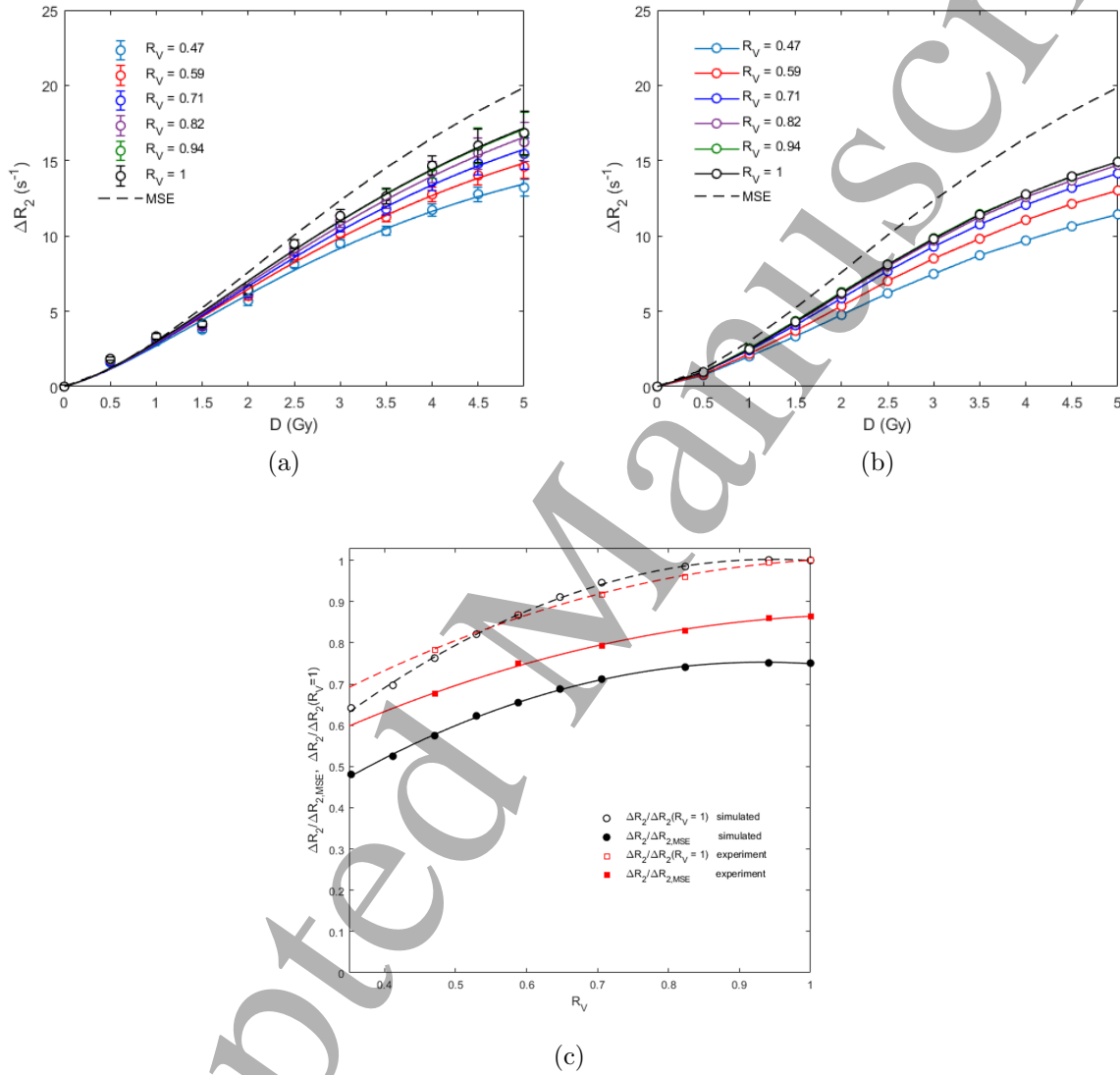
the simulations.

Figure C3: ΔR_2-dose plots acquired on the 3T MRI scanner (a) and simulated with the Bloch simulator (b) for different transmit voltage attenuations R_V and with an echo time of 168 ms. The dashed line corresponds with the MSE measured ΔR_2 values. The ratio of ΔR_2 obtained with deviating transmit voltage and ΔR_2 obtained with ideal RF pulses is shown in c as open symbols for both simulated (open black circles) and experimental data (open red squares). The ratio of ΔR_2 obtained with deviating transmit voltage and ΔR_2 acquired with the MSE sequence is shown as solid symbols for both simulated (closed black circles) and experimental data (closed red squares).

The deviation in ΔR_2 as a function of the transmit voltage deviation R_V follows a

4D Radiation Dosimetry 58

similar trend, but in comparison to the ΔR_2 values acquired with the MSE sequence, an additional offset can be observed (figure C3c) between simulated and experimental

875 data. This can be attributed to differences between the simulated sequence on the 3T MRI scanner and the simulated pulse sequence as implemented on the MRI-Linac.

On Siemens MRI scanners, the required transmit voltage can be reduced by switching from 'Normal' mode to 'Low SAR' mode in the sequence menu. This increases the duration of the RF pulses which results in a smaller demand on the

880 RF power (or transmit voltage) delivered to the coil. Switching from 'Normal' to 'Low SAR' mode, increases the duration of the excitation pulse with a factor 1.375 and the refocussing pulse duration with a factor 1.5. In the assumption that the excitation RF pulse voltage in the 'Low SAR' mode would correspond to an ideal 90 degree RF pulse, the pulse sequence in the 'Normal' mode would correspond to an RF

885 pulse scheme of $85_x - 106_y - [98_y]_{n-1}$. In the 'Low SAR' mode the pulse sequence would be $90_x - 144_y - [110_y]_{n-1}$. The use of longer RF pulses in the 'Low SAR' mode resulted in an increase in estimated ΔR_2 values but does still not correspond to the ΔR_2 values obtained with the MSE sequence (figure C4). Both RF pulse schemes have been simulated using the Bloch simulator. A similar increase in simulated ΔR_2 is observed

890 upon switching from 'Normal' to 'Low SAR' mode, confirming the hypothesis that non-ideal transmit voltages have a significant effect on the measured ΔR_2 response. The deviations in absolute values between simulations and measured ΔR_2 in the low dose region are attributed to experimental errors.
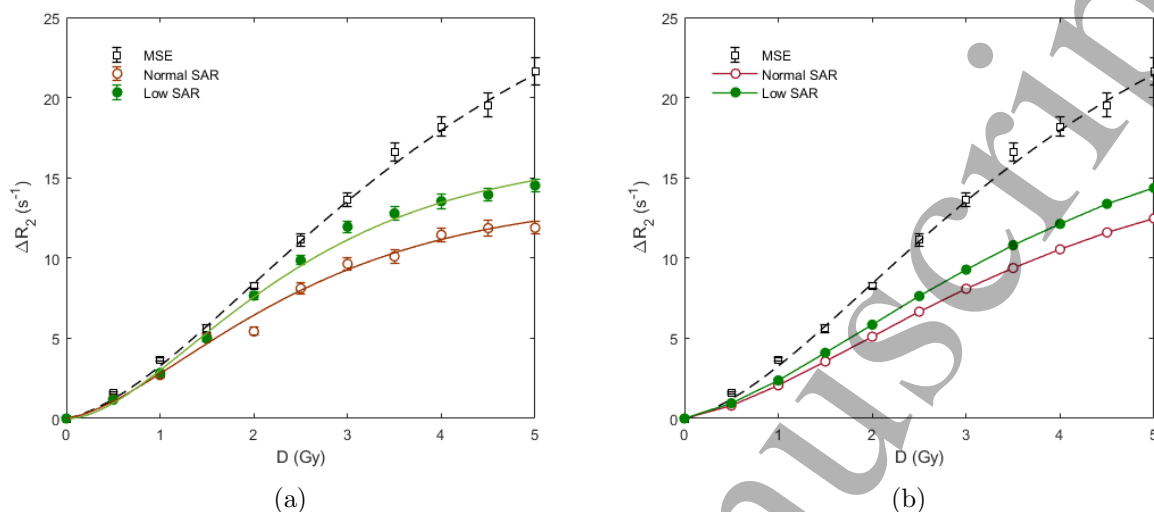
4D Radiation Dosimetry 59

(a)   (b)

Figure C4: ΔR_2-dose plots acquired on the MRI Linac with sequence in the 'Normal' mode (open circular symbols) and in the 'Low SAR' mode (closed circular symbols (a). The MSE measured ΔR_2-dose plot is shown as open square symbols and corresponding fit by a dashed line.

References

Audet C and Schreiner L J 1997 Multiple-site fast exchange model for spin-lattice relaxation in the Fricke-gelatin dosimeter *Med Phys* **24** 201-9

Baete S H, De Deene Y, Masschaele B and De Neve W 2008 Microstructural analysis of foam by use of NMR R_2 dispersion *J Magn Reson* **193** 286-96

Baldock C, Lepage M, Bäck SA, Murry PJ, Jayasekera PM, Porter D and Kron T 2001 Dose resolution in radiotherapy polymer gel dosimetry: effect of echo spacing in MRI pulse sequence *Phys Med Biol* **46**, 449-60

Baldock C , De Deene Y, Doran S, Ibbott G, Jirasek A, Lepage M, McAuley K B, Oldham M and Schreiner L J 2010 Polymer gel dosimetry *Phys Med Biol* **55**, R1:R63

Benoit-Cattin H, Collewet G, Belaroussi B, Saint-Jalmes H and Odet C 2005 The SIMRI project: a versatile and interactive MRI simulator *J Magn Reson* **173** 97-115

De Deene Y, Van de Walle R, Achten E and De Wagter C 1998 Mathematical analysis and experimental investigation of noise in quantitative magnetic resonance imaging applied in polymer gel dosimetry *Signal Processing* **70**, 85-101

De Deene Y, De Wagter C, Van Duyse B, Derycke S, Mersseman B, De Gersem W, Voet T, Achten E and De Neve W 2000a Validation of MR-based Polymer Gel Dosimetry as a Pre-clinical 3D Verification Tool in Conformal Radiotherapy: Comparison with Film Dosimetry and Computer Planning, *Magn Reson Med* **43** 116-25

De Deene Y, De Wagter C, De Neve W and Achten E 2000b Artefacts in multi-echo T_2 imaging for high-precision gel dosimetry: II. Analysis of B_1-field inhomogeneity, *Phys Med Biol* **45** 1825-39

De Deene Y, Hanselaer P, De Wagter C, Achten E and De Neve W 2000c An investigation of the chemical stability of a monomer/polymer gel dosimeter, *Phys Med Biol* **45** 859-78

De Deene Y and Baldock C 2002 Optimization of multiple spin-echo sequences for 3D polymer gel dosimetry *Phys Med Biol* **47**, 3117-41

De Deene Y, Fundamentals of MRI measurements for gel dosimetry *J Phys Conf Ser***3**, 87-114

De Deene Y, Vergote K, Claeys C and De Wagter C 2006 The fundamental radiation properties

4D Radiation Dosimetry 60

of normoxic polymer gel dosimeters: a comparison between a methacrylic acid based gel and acrylamide based gels *Phys Med Biol* **51**, 653-73

De Deene Y, Vergote K, Claeys C and De Wagter C 2006 Three dimensional radiation dosimetry in lung-equivalent regions by use of a radiation sensitive gel foam: Proof of principle *Med Phys* **33**, 2586-97

De Deene Y, Pittomvils G and Visalatchi S 2007 The influence of cooling rate on the accuracy of normoxic gel dosimeters *Phys Med Biol* **52** 2719-28

De Deene Y and Vandecasteele J 2013 On the reliability of 3D gel dosimetry *J Phy Conf Series* **444** 012015 (30 pp)

De Deene Y, Skyt P S, Hill R and Booth J T 2015 FlexyDos3D: a deformable anthropomorphic 3D radiation dosimeter: radiation properties *J Phys: Conf Ser* **60**, 1543-63

Fuxman A M, McAuley K B and Schreiner L J 2005, Modelling of polyacrylamide gel dosimeters with spatially non-uniform radiation dopse distributions *Chem Engin Sc* **60**, 1277-93.

Groenhuis V and Stramigioli S 2018 Rapid Prototyping High-Performance MR Safe Pneumatic Stepper Motors *IEEE/ASME Transactions on Mechatronics* **23**, 1843-53

Healy B J, Zahmatkesh M H, Nitschke K N and Baldock C 2002 Effect of saccharide additives on response of ferrous-agarose-xylenol orange radiotherapy gel dosimeters *Med Phys* **30** 2282-91.

Jelen U, Dong B, Begg J, Roberts N, Whelan B, Keall P and Liney G 2020 Dosimetric Optimization and Commissioning of a High Field Inline MRI-Linac. *Front Oncol* **10** 136.

Kozicki M 2011, How do monomeric components of a polymer gel dosimeter respond to ionising radiation: A steady-state radiolysis towards preparation of a 3D polymer gel dosimeter *Rad Phys Chem* **80** 1419-36

Lee H J, Kadbi M, Bosco G and Ibbott G S 2018, Real-time volumetric relative dosimetry for magnetic resonance-image-guided radiation therapy (MR-IGRT) *Phys Med Biol* **63**, 045021 (12pp)

Lepage M, Jayasakera P M, Bäck S A J and Baldock C 2001a Dose resolution optimization of polymer gel dosimeters using different monomers *Phys Med Biol* **46** 2665-80

Lepage M, Tofts P S, Bäck S A J, Jayasekera P M and Baldock C 2001b Simple Methods for the Correction of T_2 Maps of Phantoms *Magn Reson Med* **46** 1123-9

Oldham M, McJury M, Baustert I B, Webb S and Leach M O 1998 Improving calibration accuracy in gel dosimetry *Phys Med Biol* **43** 2709–20

Papoutsaki M-V, Maris T G, Pappas E, Papadakis A E and Damilakis J 2013 Dosimetric characteristics of a new polymer gel and their dependence on post-preparation and post-irradiation time: Effect on X-ray beam profile measurements *Physica Medica* **29**, 453-60

Pappas E, Kalaitzakis G, Boursianis T, Zoros E, Zourari K, Pappas E P, Seimenis I, Efstatopoulos E and Maris T G 2019 Dosimetric performance of the Elekta Unity MR-linac system: 2D and 3D dosimetry in anthropomorphic inhomogeneous geometry *Phys Med Biol* **64**, 225009

Roberts NF, Patterson E, Jelen U, Causer T, Holloway L, Liney G 2019 Experimental characterization of magnetically focused electron contamination at the surface of a high-field inline MRI-linac. *Med Phys* **46** 5780–9

Sedaghat M, Bujold R and Lepage M 2010, Impact of oxygen on the accuracy and precision of normoxic polymer gel dosimeters *J Phy Conf Series* **250** 012017 (5 pp)

Vandecasteele J and De Deene Y 2013a On the validity of 3D polymer gel dosimetry: I. Reproducibility study *Phys Med Biol* **58** 19-42

Vandecasteele J and De Deene Y 2013b On the validity of 3D polymer gel dosimetry: II. Physico-chemical effects *Phys Med Biol* **58** 43-61

Vergote K, De Deene Y, Duthoy W, De Gersem W, De Neve W, Achten E, De Wagter C 2004 Validation and application of polymer gel dosimetry for the dose verification of an intensity-modulated arc therapy (IMAT) treatment, *Phys Med Biol* **49** 287-305.

Xanthis C G, Venetis I E, Chalkias A V and Aletras A H 2014, MRISIMUL: A GPU-Based Parallel Approach to MRI Simulations, *IEEE Trans Med Imaging* **33** 607-17